# Cluster Size Effects in the Surface-Enhanced Raman Scattering Response of Ag and Au Nanoparticle Aggregates: Experimental and Theoretical Insight

Juan C. Fraire, Luis A. Pérez, and Eduardo A. Coronado*

INFIQC, Centro Laser de Ciencias Moleculares, Departamento de Fisicoquímica, Facultad de Ciencias Químicas, Universidad Nacional de Córdoba, Córdoba, 5000, Argentina

S *Supporting Information*

ABSTRACT: In this work we report the spectral evolution of the surface-enhanced Raman scattering (SERS) response of biotin molecules that generate the assembly of Ag and Au nanospheres (NSs) into clusters with controlled interparticle gaps during the aggregation process. The experiments are analyzed using rigorous near-field electrodynamic calculations of the enhancement produced in a close-packed cluster with a different number of NSs. Two kinetic mechanisms during the NS aggregation were identified which give rise to a different cluster size distribution and as a consequence to a different SERS response. It is found that during NS aggregation there is an initial fast growth of the SERS signals followed by a decay that reaches an almost constant value at relatively long times. These results are qualitatively explained by the trends observed in the electrodynamics calculations of the near-field enhancement as a function of the cluster size, which highlights the critical role played by radiation damping as the size of the cluster increases for small clusters (dimers and trimers), in contrast with the behavior observed for clusters with a relative greater number of particles where the decrease of the near-field enhancement is less significant. In addition, a general procedure is presented that makes it possible to perform a suitable comparison of the SERS response for tight-compact clusters, in the limit of large clusters, as long as the wavelength range of the SERS response is almost size independent. This procedure is tested for Ag and Au nanoaggregates generated in solution formed by spheres of different size, at an almost constant interparticle separation. It was found that even there are differences between the analytic enhancement factor and the calculated enhancement predicted by the electrodynamic theory in the large cluster size limit, and the trends in the SERS response of the biotin molecules are qualitatively explained by the electromagnetic (EM) mechanism for both Ag and Au clusters. These discrepancies could be indicative of a chemical contribution to the global SERS response, but a rigorous assessment of this mechanism would require additional theoretical calculations supported by experiments. Notwithstanding, the SERS enhancement results obtained with noncovalent bonded dye molecules (Coumarin 440 and Rhodamine B) that are randomly distributed in the clusters as Raman reporters, using the same large clusters as substrates (linked by biotin molecules), are in fairly good quantitative agreement with the electrodynamics model of the average SERS enhancement.
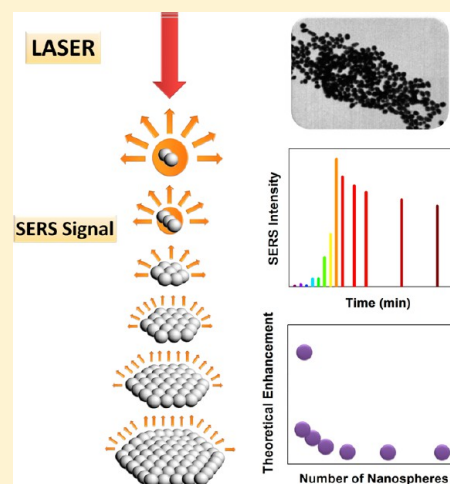
INTRODUCTION

Understanding the factors that control the degree of enhancement of confined fields around noble metal nanoparticles (NPs) and nanoaggregates is a topic of great current interest, as it is the main mechanism associated to many enhanced spectroscopies such as surface-enhanced Raman scattering (SERS),[1] tip-enhanced Raman spectroscopy (TERS),[2] surface-enhanced fluorescence (SEF),[3] etc. In particular, the huge enhancement factors enabled by SERS have led to the possibility of detecting very few molecules or even single molecules.[4] The substrates used for SERS—initially electrochemically roughened silver electrodes—have evolved over time from deposited metal films, random nanoparticle aggregates,[5−10] to rationally designed nanostructures,[11−16] and most recently to single metal nanoparticles.[12,17−20]

SERS is a plasmonic phenomenon based on the optical properties of noble metal NPs which supports localized surface plasmons, associated with the collective oscillation of the conduction electrons of the nanoparticle, the so-called localized surface plasmon resonance (LSPR). The collective excitation near the plasmon resonance induces an enhanced electromagnetic field surrounding the metallic nanoparticle with a spatial distribution that depends for a given metallic nanostructure on its geometry, its orientation with respect to the incident polarization, illumination wavelength, and dielectric environment. In addition, the LSPR frequencies can

Scheme 1. Synthetic and Theoretical Scheme Showing the Nanogap Engineering for the Generation of Nanosphere Aggregates and the Different Sphere's Cluster Configurations Simulated[a]
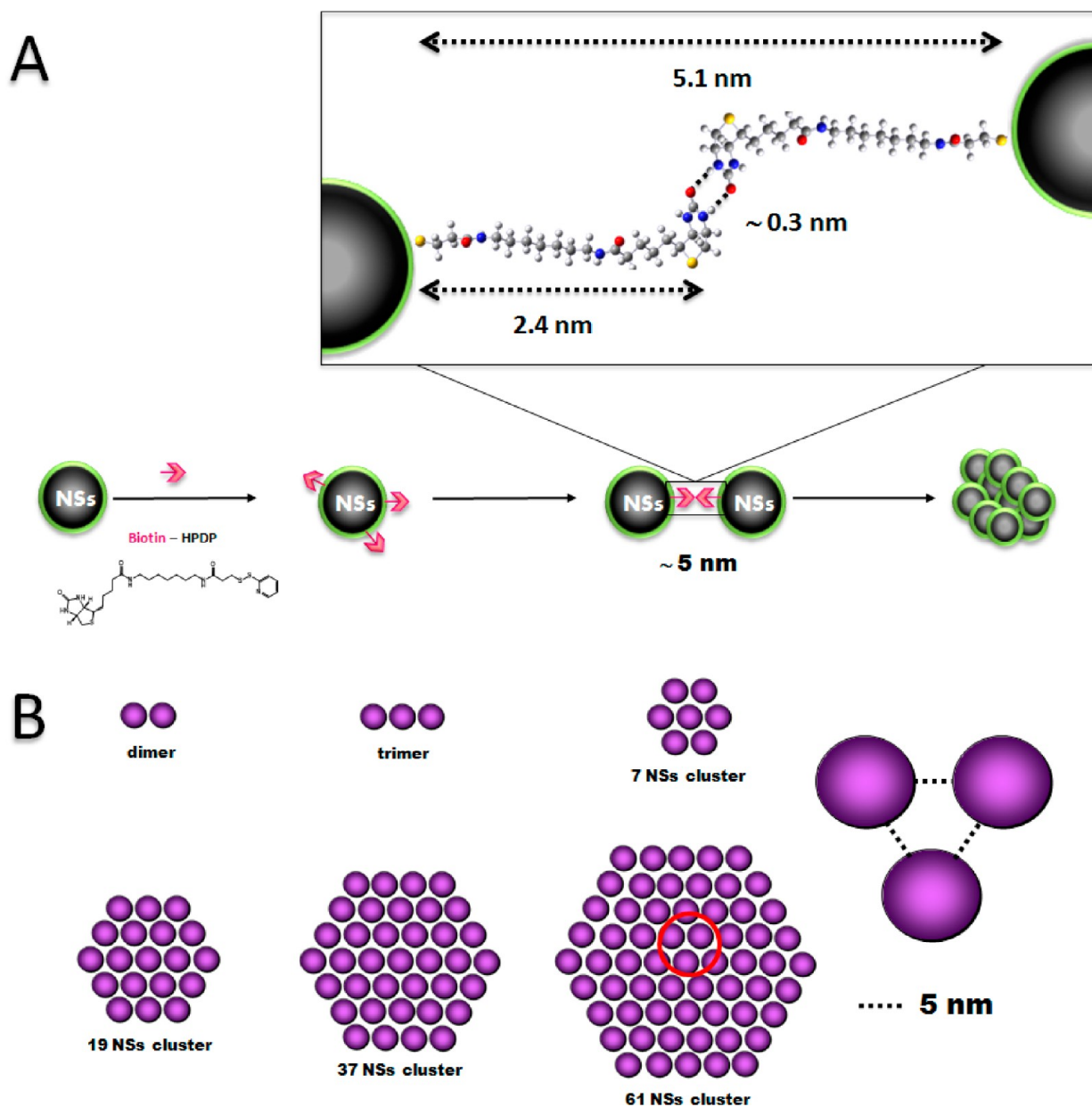
[a]A: Directional assembly of asymmetrically functionalized NSs into random structures with an interparticle gap of around 5 nm, using a biotin/NSs 1:1 molar ratio. The distances were estimated using quantum mechanical calculations (see Materials and Methods section). B: Selected sphere compact nanocluster configurations for the simulation of the far and near optical properties. All interparticle distances (gap) were fixed to 5 nm.

be tuned changing geometrical parameters, such as nanoparticle size,[21] shape,[21,22] crystal face,[23] surface roughness,[24] and interparticle spacing.[25−30]

As mentioned above, it is widely accepted that the major contribution to SERS signals comes from the electromagnetic (EM) enhancement, caused by LSPR excitations. Another mechanism often argued to explain SERS is the chemical one, but this mechanism has proved to have by far a lower contribution.[31] Furthermore, it is well-known that the EM field around metal nanoparticle aggregates is amplified in a nonuniform way as a consequence of plasmon coupling. This coupling gives rise to the so-called hot spots generated within the nanoparticle gaps.[32−35] The strong interactions of plasmons in NP assemblies can render possible many useful applications

including SERS bio(nano)sensors and also nanoparticle waveguides.[36]

Although particles with sharp features can provide high near-field enhancement, most of the reports of the strongest SERS signals achieved come from NP clusters.[5,7,30] Calculations of the field strengths in the coupling region between adjacent NPs typically reveal that interparticle fields are many orders of magnitude greater than the fields at the surface of single nanoparticles. Although gaps play a key role in the surface-enhancing properties of NP clusters, the electromagnetic contribution to SERS in this particular type of nanostructures is a topic that still remains to be further investigated.

The SERS activity observed in metal NP aggregates is often rationalized by considering only the interaction of two neighbor

NPs, i.e., using dimer models. A more rigorous model should be to consider the interaction of the LSPR of all the particles of the aggregate, i.e., a many-particle model.[37,38] This fact focused our attention on the validity of the implementation of a dimer model to correlate the experimental SERS behavior of NP aggregates.

The expected theoretical electromagnetic SERS enhancement, for small Raman shifts, scales with the fourth power of the field, while for Raman shifts that are significantly greater than the width of plasmon resonance local electromagnetic SERS enhancement scales with the product of the field intensity enhancements at the incident and scattered frequencies.[31] Considering that upon optical excitation of the LSPR of metallic nanoparticles and nanostructures the maximum near-field enhancements occur at lower energies than the maximum of the extinction in the corresponding far-field spectrum,[39] evaluating the variation of the maximum enhancement at a particular excitation wavelength as the number of NPs in the aggregate increases is crucial for a rational design of SERS substrates.

Despite that there is a great number of studies dealing with the SERS performance of NP dimers,[11,17,28,29,40−43] there are only a few theoretical studies devoted to investigating the optical properties of NP aggregates as a function of the aggregate size, and to the best of our knowledge all these studies were performed with aggregates deposited or generated on a substrate.[20,44−48] In a previous work Taylor et al. studied the SERS response of growing Au nanosphere aggregates in solution.[49] Nevertheless, more detailed studies focused on correlating the evolution of the experimental Raman signal as metal clusters grow with theoretical simulations are still needed.

The goal of the present work is to identify trends in the magnitude of the SERS signal as a function of the aggregate size for silver and gold spherical NP aggregates. In particular, we have investigated the evolution of the SERS signals during aggregation induced by biotin molecules in colloidal solutions of 56 nm silver and 90 nm gold NSs. In addition, we have correlated the analytical enhancement factors (AEFs)[50] with the theoretical enhancement factors as a function of cluster size at a constant excitation wavelength (488 nm for Ag and 633 nm for Au experiments, respectively). These wavelengths were chosen because, as it will be shown later, in this wavelength range a regular behavior of the enhancement with cluster size is achieved; i.e., at these wavelengths the enhancement predicted by electrodynamics theory quickly decreases with cluster size until it reaches an almost constant asymptotic value. This feature is important since as soon as a critical value of the cluster size is reached the electromagnetic contribution is almost the same; therefore, detailed knowledge of the cluster size distribution is not needed to evaluate the electromagnetic contribution to the SERS enhancement.

The generation of aggregates involves the biotinylation of Ag and Au nanospheres (NSs) by the addition of "activated" Biotin (molar ratio 1:1 biotin/NSs), which gets chemisorbed onto the surface of the NSs. The "activation" of biotin was performed by a thiol exchange reaction with mercaptoundecanoic acid (MUA), with a 1:10 biotin/MUA ratio. Using this procedure (see below) there is on average one biotin per nanoparticle in all the experiments, and the interaction of the biotinylated NSs leads to the formation of close-packed aggregates through H bonds between biotins, with an interparticle gap of around 5 nm (Scheme 1A).

The variation of the SERS signals during the aggregation process was rationalized theoretically using selected close-packed nanoclusters with 5 nm interparticle distance. To estimate the role of the cluster configuration in the near-field enhancement factors, we have also calculated (using the generalized multiparticle Mie theory (GMM theory)) the angular average near-field enhancement achieved at different wavelengths for nanoclusters with increasing number of NSs (2, 3, 7, 19, 37, and 61 NSs) to rationalize the experimental SERS enhancement (Scheme 1B). The selected configurations were chosen by inspection of the TEM images, as will be shown below. The results show that the theoretical average enhancement decreases with cluster size until reaching an almost constant asymptotic value for both Ag and Au clusters.

Finally, the experimental AEF achieved for relatively large aggregates is compared with the theoretical angular average enhancement factor for a 61 NS cluster. The role played by slight variation of the cluster geometries (the interparticle gap and the presence of vacancies in the structure of the cluster) in the calculated angular average enhancements as well as the variation of the near-field distribution as a function of the enhancement factor have been also analyzed. It was found that the SERS enhancement given by the theoretical simulations is a factor of 10−100 smaller than that obtained experimentally for the biotin molecules for the larger aggregates (formed once an asymptotic value of the experimental SERS has been achieved). This result could be indicative of chemical contribution to the SERS enhancement. In contrast, the average enhancement predicted by theory is in very good agreement with the SERS enhancements experimentally obtained adding dye molecules (Cumarin 440 and Rhodamine 6G) to the same cluster solution, demonstrating that the EM mechanism is able to account for the experimental observations within experimental error.

■ MATERIALS AND METHODS

Materials. The following materials were used as obtained: $HAuCl_4$ (Carlo Erba); $AgNO_3$ (Blaker); sodium citrate (Mallinckrodt); EZ-Link biotin-HPDP (Pierce); rhodamine B (Exciton); coumarin 440 (Exciton).

Nanosphere Synthesis. The synthesis of gold and silver nanoparticles was performed using the Turkevich method, which is based on the reduction properties of boiling citrate solutions. Au nanoparticles were produced by reducing a 50 mL 0.2 mM chloroauric acid solution ($HAuCl_4$) with the addition of 0.5 mL of a 0.01 M citrate solution (corresponding to a 1:0.5 Au/Citrate molar ratio) under heat and rapid stirring for 30 min. Ag NSs were obtained through a similar procedure as described above but using a 1:1 Ag/citrate molar ratio. The morphological characterization of the Au and Ag NSs was performed combining UV−vis spectroscopy, TEM, dynamic light scattering (DLS), and electrodynamic modeling using Mie theory. The overall results after combining all of these different techniques and modeling indicate that the average diameter was 90 nm with a picomolar concentration of 4.36×10^9 NSs/cm^3 (7.24×10^{-12} M), for Au NSs, and was 56 nm with a concentration of 4.57×10^9 NSs/cm^3 (7.59×10^{-12} M) for Ag NSs. The concentration of the Au and Ag nanoparticles was estimated to be around 7 pM, using the experimental extinction intensities at the maximum wavelength and Mie theory calculations of the extinction cross section for spherical particles with the corresponding diameter (determined by TEM).
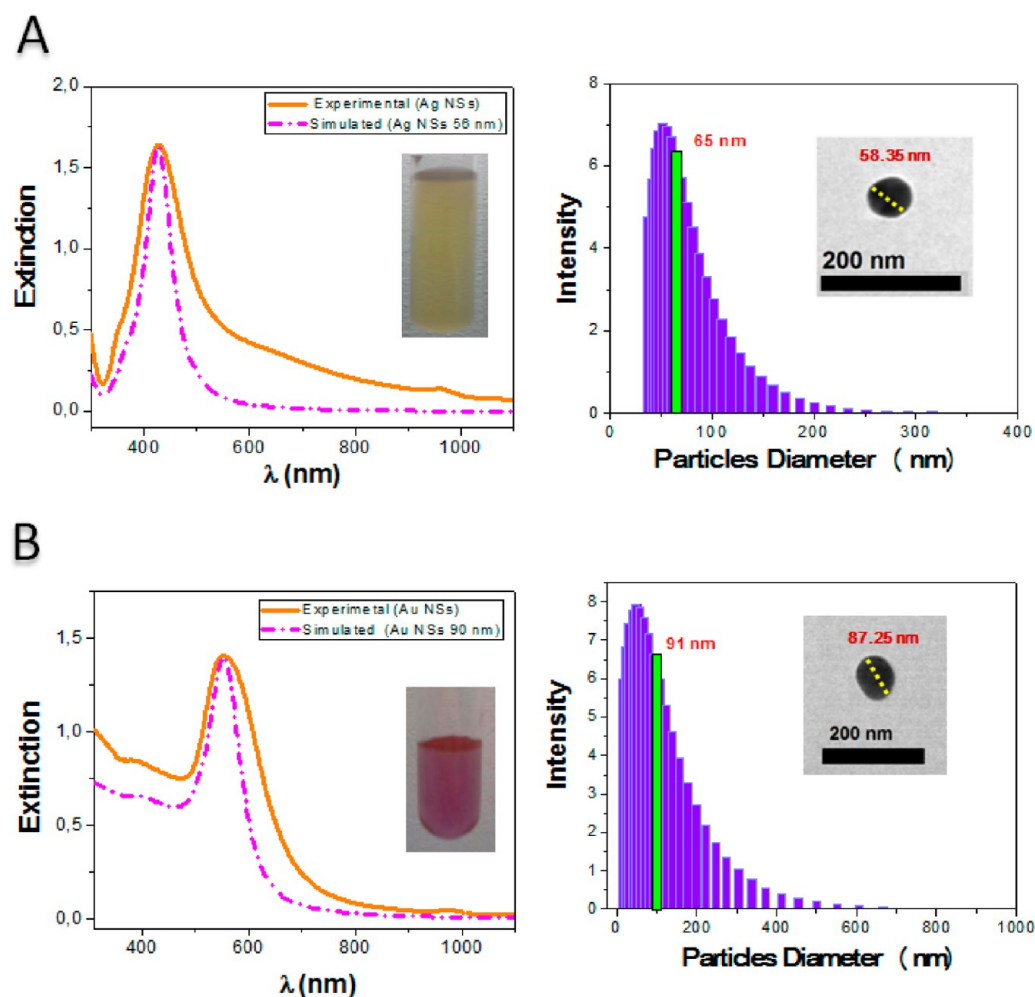
23092

dx.doi.org/10.1021/jp3123709 | J. Phys. Chem. C 2013, 117, 23090−23107

Figure 1. Optical and morphological characterization of Ag and Au NSs. Calculated (dashed lines) and experimental (solid line) extinction spectrum (left column) and the corresponding DLS histogram and TEM images (right column) for (A) 56 nm diameter Ag NS colloidal dispersion and (B) 90 nm diameter Au NS colloidal dispersion. All the extinction spectra have been calculated using Mie theory.

Nanoparticle Surface Funcionalization. EZ-Link Biotin-HPDP (N-[6-(biotinamido)hexyl]-3′-(2′-pyridyldithio)-propionamide) was used for surface functionalization of both Au NSs and Ag NSs. The procedure for the generation of close-packed aggregates consists of the incubation at room temperature of 30 mL of NS colloidal dispersion in the presence of EZ-Link Biotin-HPDP (molar ratio NS/biotin 1:1).

In all cases biotin was previously "activated" by reaction with mercaptoundecanoic acid (MUA), with a 1:10 biotin/MUA ratio.

Extinction Measurements. The characterization of the extinction properties of the Ag NS and Au NS colloidal dispersions was carried out by UV−vis spectroscopy in the 300−1100 nm wavelength range using a Shimazdu UV-1700 PharmaSpec spectrophotometer with a 1 cm quartz cell at room temperature.

DLS Measurements. The dynamic light scattering (DLS) characterization of Ag NS and Au NS colloidal dispersions was performed using a Delsa Nano 2.2 spectrometer with a 1 cm quartz cell at room temperature.

Electron Microscopy. Transmission electron microscopy (TEM) images were obtained using a JEM-JEOL 1120 EXII under an accelerating voltage of 80 kV. Samples were prepared by adding one drop (∼50 μL) of the sample colloidal solution

onto a holey carbon-Formvar coated copper TEM grid (300 mesh).

SERS Measurements. SERS measurements were performed using a Horiba LabRaman confocal microscope with a 5× (NA = 0.12) length in the backscattering geometry. The spectra acquisition time was 10 s for measuring the SERS evolution during NS aggregation and was 20 s for determining the analytic enhancement factor (AEF) at the end of NS aggregation. The spectra were acquired with a 600 lines mm^{-1} grating, giving a resolution of 4 cm^{-1}. The excitation wavelengths used were the 488 nm line from an argon laser for Ag experiments and the 633 nm line from a He−Ne laser for Au experiments. All measurements were performed at room temperature and were calibrated to Si and to H$_2$O bands in the colloidal solutions.

Computational Methods. The optical response of Ag and Au NS clusters was computed using the generalized multi-particle Mie theory (GMM) as described elsewhere.[51−53] In all near-field calculations presented in this work the dielectric function tabulated by Palik for Au and Ag was employed.[54] For each cluster analyzed, the separation parameter between the nanospheres is large enough so that nonlocal effects on the dielectric constant can be neglected. For the calculations of the cluster, near-field properties were used of a multipolar order of 20. Three different average enhancement factors have been
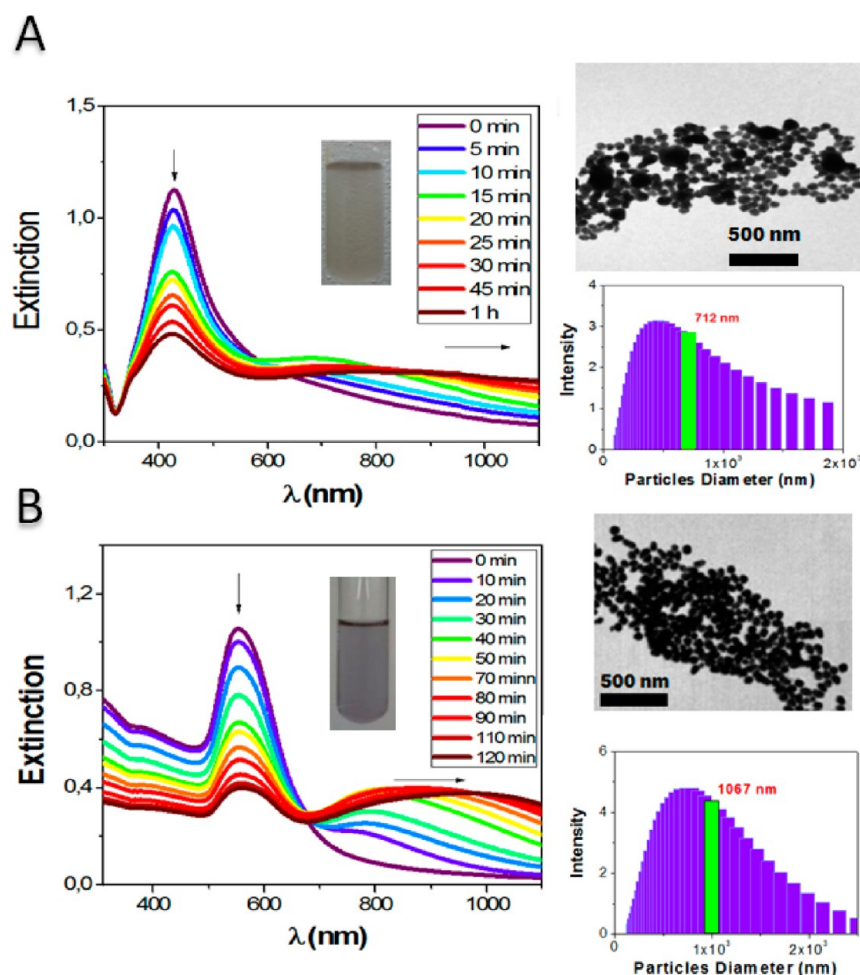
Figure 2. Optical and morphological characterization of NS random aggregates. Evolution of the extinction spectra at different times (indicated in the inset of each figure) during NS aggregation (left column) and the DLS histogram and TEM images (righ column) for (A) 56 nm diameter Ag NS and (B) 90 nm diameter Au NS aggregates. The arrow at shorter wavelengths in the extinction spectra indicates the decrease of the extinction intensity at the monomer LSPR band, and the arrow at longer wavelengths denotes the red shift of the aggregate's collective resonance mode. The representative TEM images of the tight-compact random aggregates generated and the DLS were acquired after 1 and 2 h of the addition of biotin for the Ag and Au colloidal dispersion, respectively. The vertical green lines in each DLS histogram indicate the average size of the aggregate.

computed: angular average denoted by $\langle\Gamma(\omega)\rangle_\theta$ averaged over 18 different polarizations (from 0° to 170° at 10° steps), angular average considering vacancies in the nanostructure denoted by $\langle\Gamma(\omega)\rangle_{\theta,v}$ which considers simultaneously the average over different polarizations and the variation of the cluster geometry by generating vacancies in the cluster in a random way, and $\langle\Gamma(\omega)\rangle_{\theta,v,d}$ which takes into account simultaneously the average over different polarizations of the cluster geometry by generating vacancies and the variation of the gap distance between 4 ± 1 nm.

Quantum Chemistry Calculations. Ab initio calculations were performed with the Gaussian 98 program suite.[55] In all calculations, we use Becke's three-parameter hybrid functional method using Lee−Yang−Parr correlation functional (B3LYP) methods with 6-311++G(d,p) basis sets.

■ RESULTS AND DISCUSSION

Far-Field Optical and Morphological Characterization of NSs and Aggregates. The left column of Figure 1 depicts the experimental extinction spectra (solid line) of the Ag (Figure 1A) and Au (Figure 1B) NS colloidal dispersions and the corresponding simulated spectrum using GMM theory (dashed lines). Details of how to calculate the far as well as the near-field properties of NS aggregates can be found elsewhere.[51−53] As it can be noticed, in both cases the correlation of experimental and theoretical extinction spectra is satisfactory, regarding the peak position of the LSPR wavelength. This feature indicates that nearly spherical nanoparticles are obtained in the NP synthesis, with average diameters of 56 and 90 nm for Ag and Au NSs, respectively, as can be seen in the transmission electron microscopy (TEM) images (right column of Figure 1). The differences observed with respect to the peak width are due to inhomogeneous size broadening as it could be appreciated in the dynamic light scattering (DLS) histograms (right column of Figure 1). Note that DLS signals shown in Figure 1 are in intensity units, and therefore, they are proportional to the scattering cross section of the clusters. As the scattering cross section scales, in the quasi-static limit, with the sixth power of size, larger particles will have very high scattering intensities even if their concentration is very low compared with that of the smaller particles (i.e., a particle being 10 times greater in size will have a million times greater scattering cross section).[56] Therefore, even if the DLS signals are spread over a relatively large size distribution, the mean diameter agrees quite well with the mean diameter obtained by TEM and with the electrodynamics simulations.

Now let us analyze the optical behavior of close-packed NS aggregates with controlled interparticle distances generated using biotin molecules as linkers, using the already characterized colloidal spectrum of Ag and Au NSs. The spectral change of the colloidal dispersions at different times after the addition of biotin (final concentration of 7.59×10^{-12} M and 7.24×10^{-12} M for Ag and Au, respectively) is shown in the left column of Figure 2. The most significant feature to be noticed is the appearance of a second band at longer wavelengths which gradually red shifts and broadens as time elapses. This band in the extinction spectrum which suffers an important shift at longer wavelengths will be denoted hereafter as "collective mode of the aggregate" as it is the one whose red shift clearly denotes NP aggregation.[37] The formation of close-packed aggregates after 1 h of reaction time with biotin for Ag NSs and 2 h of reaction time for Au NSs was confirmed by TEM and by DLS experiments. The DLS results indicate the formation of Ag NS aggregates with an average size of 712 nm (see DLS histogram in the right column of Figure 2A). The TEM images show that these aggregates have a tight-compact structure (close-packed clusters), and they can be considered formed by small pseudospherical clusters. For Au NS aggregates, the DLS results (histogram in the right column of Figure 2B) indicate that their average size is 1067 nm, while the TEM images show that these aggregates are also close-packed clusters formed by pseudospherical clusters. A close inspection of the TEM images reveals that this is indeed the case, as the large aggregate can be considered to be formed by the superposition of smaller aggregates having regular structures indicated by the colored circles in Figure 3A. The idealized cluster configuration associated to each structure is depicted in Figure 3B. As will
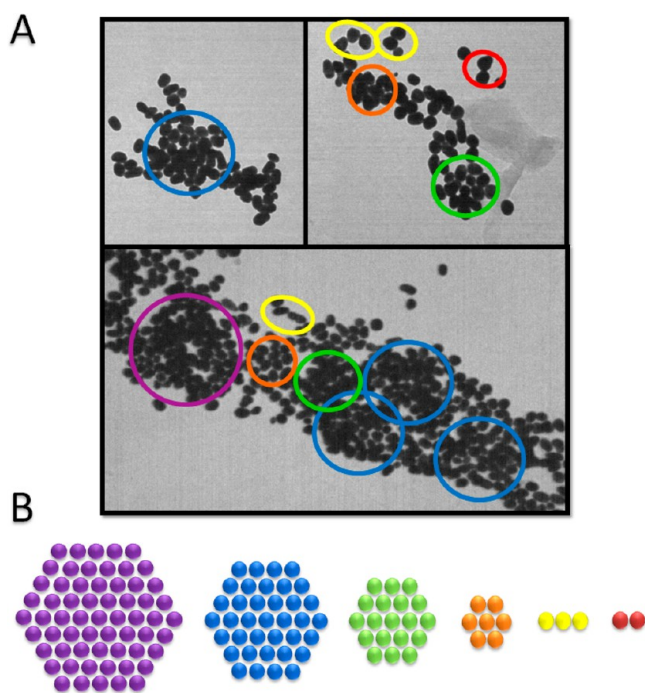
be discussed below, this assumption probes to be quite suitable to explain the optical behavior of the system.

The interparticle gap was estimated from structural chemical considerations which are supported by quantum mechanical calculations that allow obtaining an optimized structure of the biotin fragment of the analyte used for the aggregation, which extended is around 2.4 nm in length. Considering the fact that an average H-bond length is in the order of 0.3 nm, the total length could be estimated to be around 5 nm (upper limit). This distance could not be determined by the conventional TEM technique used in the present work, as there could be an overlap of the TEM images of the NPs projected on the plane of the substrate due to their faceted nature,[57] and the distances under vacuum should be shorter than that of particles in solution.[58]

Far- and Near-Field Theoretical Optical Characterization of Closed-Packed NS Clusters. As discussed above, biotin induces aggregation with a controlled separation (around 5 nm) between NSs. In this section we will analyze by rigorous electrodynamics modeling using GMM theory the trends in the near- and far-field optical properties of some selected close-packed configurations (see Scheme 1B and Figure 3) containing a different number of Ag and Au NSs. In particular we will examine the variation of the extinction spectra and the distribution of the near field with cluster size, in order to rationalize the SERS response of Ag and Au biotinylated NS aggregates. Let us first consider simulations performed in aqueous solution (dielectric constant = 1.77) with an incident polarization chosen in such a way as to give the maximum interparticle plasmon coupling; i.e., the electric field oscillates along the cluster plane. The enhancement factor at a particular frequency ($\Gamma(\omega)$) is defined by the square power of the ratio between the enhanced field (E) in the cluster and the incident field (E_0): $\Gamma(\omega) = |E(\omega)/E_0(\omega)|^2$.

Figure 4A shows the variation of the extinction spectra of 56 nm Ag NS aggregates as a function of cluster size for the representative cluster geometries depicted in Scheme 1B. The monomer spectrum shows the characteristic peak for Ag NS LSPR dipole mode at 427 nm, which strongly red shifts (from 427 to almost 985 nm) as the number of Ag NSs increases. Another important feature to be noticed is the appearance of additional multipolar LSPR bands as the complexity of the cluster increases. As a consequence, the spectrum broadens and red-shifts as the number of NSs increases. This behavior is in agreement with the measured spectral evolution of biotinylated Ag NSs during aggregation (see Figure 2A), which gradually shows the appearance of aggregate modes at longer wavelength increase its intensity and broadens during NP aggregation.

The variation of the maximum $\Gamma(\omega)$ values (achieved in the interparticle gaps) as a function of the wavelength (hereafter denoted as "maximum near-field enhancement spectrum", MNFES) for the different selected Ag NS cluster geometries is shown in Figure 4B. Note that at constant interparticle separation the highest near-field enhancement is achieved in dimers. Increasing the number of NSs in the cluster gives rise to a red shift and broadening of the MNFES, the same trend observed in the extinction spectra. However, it is worthwhile to remark that the MNFES is red-shifted with respect to the extinction one, a feature already explained by Nordlander et al. in terms of intrinsic damping and radiation damping.[39]

The MNFES depicts a shift of around 50 nm in its maximum value as the number of NSs increases for the different clusters simulated until the MNFES of the 7 NS cluster that does not

Figure 3. Electrodynamics modeling of the experimental close-packed clusters. (A) Representative TEM images of 90 nm Au NS close-packed clusters. The circles with different colors identify specific cluster configurations with different number of NSs. (B) Selected sphere's tight-compact structure configurations simulated.
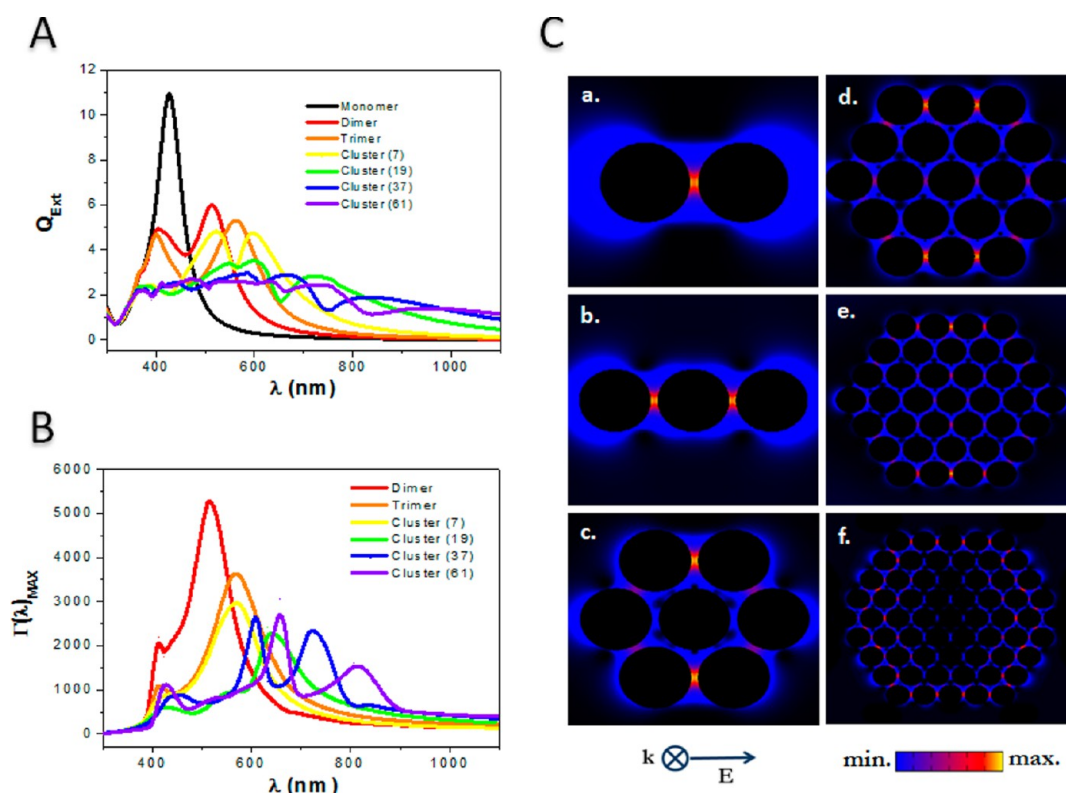
Figure 4. Far- and near-field optical characterization of 56 nm Ag nanoclusters. (A) Simulated extinction efficiency (Q_{EXT}), (B) simulated maximum near-field enhancement spectrum (MNFES) ($\Gamma(\lambda)_{MAX} = |E(\lambda)/E_0(\lambda)|^2_{MAX}$), and (C) spatial distribution of E-field enhancement at 488 nm for the selected 56 nm Ag sphere compact nanocluster configurations (indicated in the inset of graphic B). The numbers of NSs in each calculation are indicated in the respective insets of (A) and (B).

experience a red shift with respect to the maximum of the trimer but a significant decrease in its intensity. The larger cluster (19, 37, and 61 NS clusters) depicts a shift of around 80 nm in its maximum value as the number of NSs increases. These features, in conjunction with those observed also for Au NS clusters, have important implications in experiments where the SERS substrate is a NP aggregate, as the maximum enhancement value is reached at different wavelengths depending on the number of NSs in the cluster.

Figure 4C depicts the spatial distribution of the square power of the enhanced field at 488 nm (experimental irradiation wavelength) for the selected Ag NS cluster configurations, with perpendicular incident polarized light with respect to the cluster plane and electric field polarized along the dimer interparticle direction. Note that the spatial distribution of the enhancement is symmetrical with respect to the cluster axis and that the hot spots are located at the top and bottom edges for large clusters.

Calculations performed with 90 nm Au NS clusters show a similar behavior to that observed for Ag NS clusters, i.e., a complex extinction spectra that broadens and drops in intensity as the cluster increases its size (see Figure 5A). The monomer spectrum shows a single peak at 562 nm, while for larger clusters (7 NSs to 19 NSs clusters) the spectra clearly red shift with an increasing number of peaks due to plasmon coupling that gives rise to several resonance wavelengths in the range 668−1067 nm.

The MNFES for Au clusters (see Figure 5B) have a significant difference from that observed for the Ag NS clusters; i.e., there is a red shift in the enhancement maximum of almost 100 nm from dimer to trimer and only a shift of 50 nm from

the dimer to 7 NS cluster. The red shift for the 7 NS cluster and the larger clusters simulated is around 180 nm considering the band at higher wavelengths. This band cannot be observed in the case of the 61 NS cluster as it is out of range. The major difference between the enhancements generated in Ag and Au clusters is that, although Ag NSs are almost half the size, the smaller clusters (dimers) give rise to slightly higher field enhancements in Ag than in Au clusters. Note that in the case of Au clusters at constant interparticle separation the highest near-field enhancement is achieved for the 37 NS cluster at 822 nm, while for Ag clusters the maximum enhancement is achieved for dimers at 517 nm (see Figure 5B and Figure 4B, respectively).

The spatial distribution of the square power of the field enhancement at 633 nm (experimental irradiation wavelength) for the selected Au NS clusters is shown in Figure 5C. Quite remarkably, for large clusters the distribution pattern of the hot spots is very similar when comparing Au and Ag clusters of the same number of spheres at the two excitation wavelengths used. These calculations indicate that for these wavelengths and for large clusters some different spatial regions of maximum enhancement in a cluster could be preferentially excited. Another feature to be remarked with respect to the near-field distribution is that the gaps with the greatest enhancement are located mostly in the outer sphere shell of the clusters (according to the polarization direction).

By comparing the extinction spectra of both Ag and Au clusters (see Figures 4A and 5A) with the corresponding MNFES (see Figures 4B and 5B), several features may be noticed. First, as has been found in previous studies, the peak positions of the MNFES are not located at the same
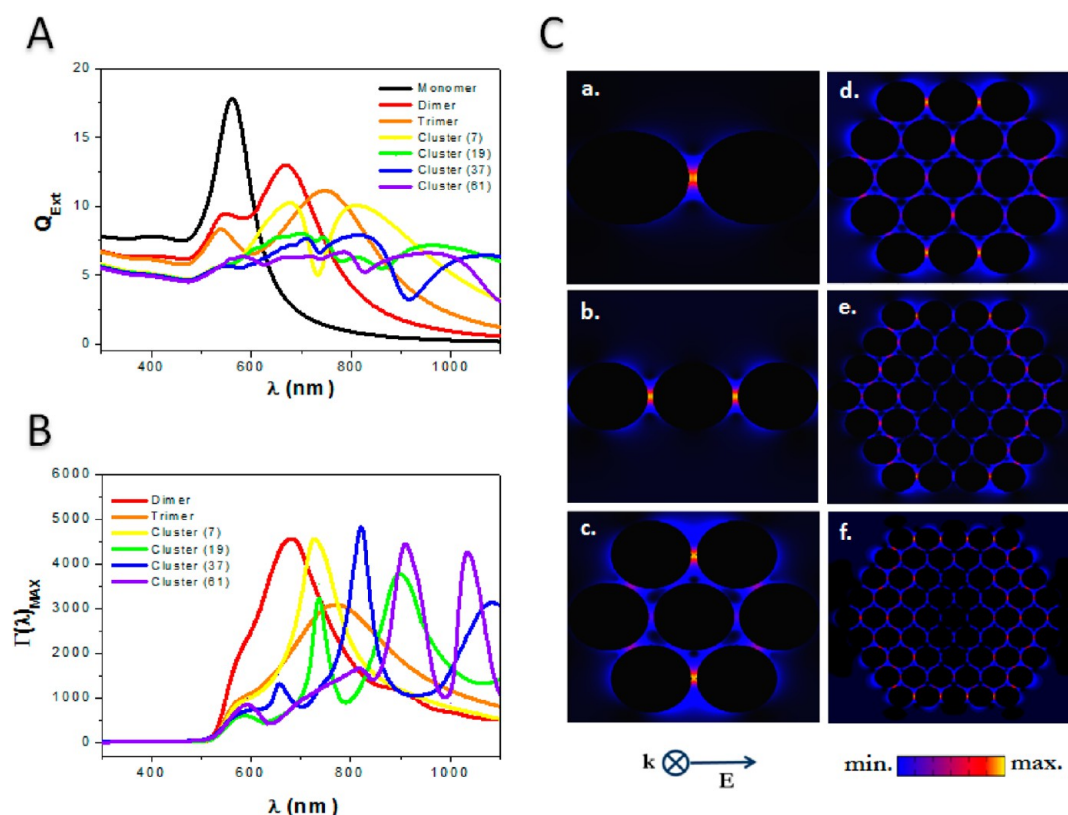
Figure 5. Far- and near-field optical characterization of 90 nm Au nanoclusters. (A) Simulated extinction efficiency (Q_{EXT}), (B) simulated maximum near-field enhancement spectrum (MNFES) ($\Gamma(\lambda)_{MAX} = |E(\lambda)/E_0(\lambda)|^2_{MAX}$), and (C) spatial distribution of E-field intensity enhancement at 633 nm for the selected 90 nm Au sphere compact nanocluster configurations (indicated in the inset of graphic B). The numbers of NSs in each calculation are indicated in the respective insets of (A) and (B).

wavelengths of the extinction spectra.[39] Second, the global shape of the extinction spectra does not follow the MNFES. In general, the MNFES as a whole is red-shifted with respect to the extinction spectra; i.e., the onset of the range of wavelengths where a significant enhancement is achieved is displaced several nanometers with respect to the extinction spectra. This points out that the sometimes intuitive invoked argument that the region of maximum near-field enhancement should be quite in the position of the maximum of the extinction spectra is not correct. The magnitude of the enhancement for individual NPs, where only one mode is involved, could be rationalized in terms of the intrinsic damping that depends on the imaginary part of the dielectric constant of the metal and the extrinsic damping that is proportional to the NP polarizability, which increases with the sphere radius.[39] For clusters the situation is more complicated as there are several factors that may produce complex interference of the several multipole plasmon modes that are involved and also Fano-type interactions that make the analysis very complex. There is also an interplay between intrinsic damping (which increases with the magnitude of the imaginary part of the dielectric constant) and the extrinsic radiation damping (which increases with the cluster size for a constant interparticle separation) in determining the magnitude of the enhancement. The larger the intrinsic or the extrinsic damping, the smaller the magnitude of the field enhancement should be.

The variation of the maximum $\Gamma(\omega)$ at a constant wavelength as a function of the cluster size for silver and gold aggregates shows different trends depending on the excitation wavelength (see Figure S1 in the Supporting

Information). Therefore, to make a suitable comparison between theory and experiments, we have chosen two excitation wavelengths in our experiments ($\lambda = 488$ nm and $\lambda = 633$ nm for Ag and Au experiments, respectively) where the variation of the maximum enhancement with cluster size is similar for both types of metals. In that sense, after a critical number of spheres, it decreases with cluster size until it reaches an almost constant value. As discussed above there is an intrinsic damping (which is only determined by the imaginary part of the dielectric constant of the metal) at the particular excitation wavelength. This intrinsic damping explains why Au clusters have almost the same enhancement factor as Ag as the imaginary part of the dielectric constant of gold is only slightly greater at 633 nm than for Ag at 488 nm. On the other hand, there are also extrinsic size effects, i.e., the radiation damping mechanism which increases with the volume of the whole cluster. The slightly asymptotic decrease of the number of hot spots observed on increasing the size is probably due to electrodynamic effects: by increasing the aggregate size the quantity of radiation scattered by the system increases, and thus the energy available to create hot spots decreases. Hence, there is no point in using experimentally metal clusters that are too large in size.

However, as it has been pointed out above, the fact that beyond a critical size the electromagnetic field enhancement is independent of the cluster size considerably simplifies the comparison between theory and experiments because the electromagnetic SERS enhancement is now independent of the cluster size distribution.
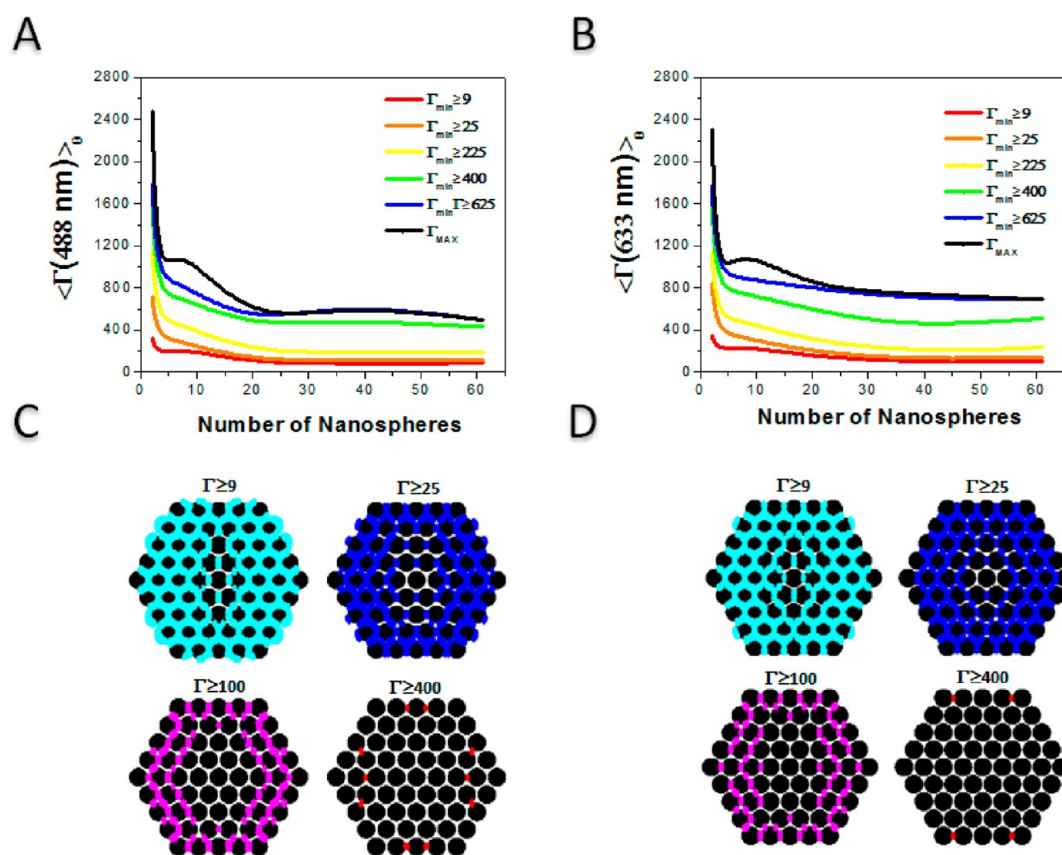
Figure 6. Near-field optical properties of 56 nm Ag clusters and 90 nm Au clusters. Near-field properties of 56 nm Ag clusters: (A) comparison of the square power of the average E-field enhancement ($\langle\Gamma(488\ nm)\rangle_\theta = \langle|E(488\ nm)/E_0(488\ nm)|^2\rangle_\theta$) averaged for different polarization of the external E-field and considering different minimum values of the E-field enhancement (Γ_{min}), as a function of the number of NSs in the cluster. (C) Near-field GMM calculations of the spatial distribution of E-field enhancement at 488 nm for a 61 NS Ag compact cluster as a function of Γ_{min}. Near-field properties of 90 nm Au clusters. (B) Comparison of the square power of the average E-field enhancement ($\langle\Gamma(633\ nm)\rangle_\theta = \langle|E(633\ nm)/E_0(633\ nm)|^2\rangle_\theta$) averaged for different polarization of the external E-field and considering different minimum values of the E-field enhancement (Γ_{min}), as a function of the number of NSs in the cluster. (D) Near-field GMM calculations of the spatial distribution of E-field enhancement at 633 nm for a 61 NS Au compact cluster as a function of Γ_{min}.

Having analyzed the near-field optical behavior of Ag and Au clusters as a function of the cluster size for a single polarization and the distribution of the near-field enhancement, it is now convenient to have a more realistic comparison with experiments to analyze the variation of the angular average of $\Gamma(\omega)$ as a function of the cluster size. In addition, different angular averages ($\langle\Gamma(\omega)\rangle_\theta$) have been computed depending on the lower limit of the enhancement (Γ_{min}) used to perform the integration

$$\langle\Gamma(\omega)\rangle_\theta^{\Gamma_{min}} = \int_{\Gamma_{min}}^{\Gamma_{max}} \Gamma_i(\omega)\,di \Big/ \int_{\Gamma_{min}}^{\Gamma_{max}} di \tag{1}$$

where i corresponds to the ith point in the cluster. In all the integrations, $\langle\Gamma(\omega)\rangle_\theta$ has been calculated by taking the average value of $\Gamma(\omega)$ over 18 different polarizations. Figure 6A and B shows that $\langle\Gamma(\omega)\rangle_\theta$ decreases as the number of particles in the cluster increases, until reaching a constant asymptotic value. This behavior is independent of the lower value of Γ_{min} used for taking the average. As should be expected, increasing the lower limit of integration (Γ_{min}) increases the value of $\langle\Gamma(\omega)\rangle_\theta$ independent of the size of the cluster and for both metals. Notwithstanding, as is clear from the near-field distribution patterns shown before, these regions of highest enhancement are a small portion of the total interparticle regions of the cluster. As an example, Figure 6C and D shows the distribution

of the regions with enhancements greater than a certain minimum value. In this case, it is clearly evidenced that regions with $\Gamma \geq 9$ almost cover 100% of the interparticle region of the cluster, and as the value of Γ_{min} is increased there is a gradual decrease of this area as shown in the sequence $\Gamma \geq 9$; $\Gamma \geq 25$; $\Gamma \geq 100$; $\Gamma \geq 400$. In fact the enhancements $\Gamma \geq 400$ spread only in a small region of the cluster, in spite of being the gaps which give rise to the greatest enhancement; that is, only 1% of the total gaps have values of Γ greater than this value.

SERS Response of Ag and Au Aggregates as a Function of Cluster Size. The evolution of the biotin SERS spectra during Ag and Au NS aggregation is shown in Figure 7A and B, respectively. In both cases a similar behavior is observed: initially there is an almost exponential increase of the SERS intensity reaching a maximum value at a given time after which there is a slower decay which approaches an almost constant asymptotic value at long times.

Figure 8A and B shows the calculated SERS enhancement factor as a function of the number of NSs in the cluster for Ag NS and Au NS clusters, respectively, for the 1440 cm^{-1} (Stokes shift at $\lambda = 525$ nm for Ag and Stokes shift at $\lambda = 696$ nm for Au) vibrational mode of biotin defined as the product of the square power of the E-field enhancement at the incident frequency ($\Gamma(488$ nm) for Ag and $\Gamma(633$ nm for Au) and the square power of the E-field enhancement at the corresponding
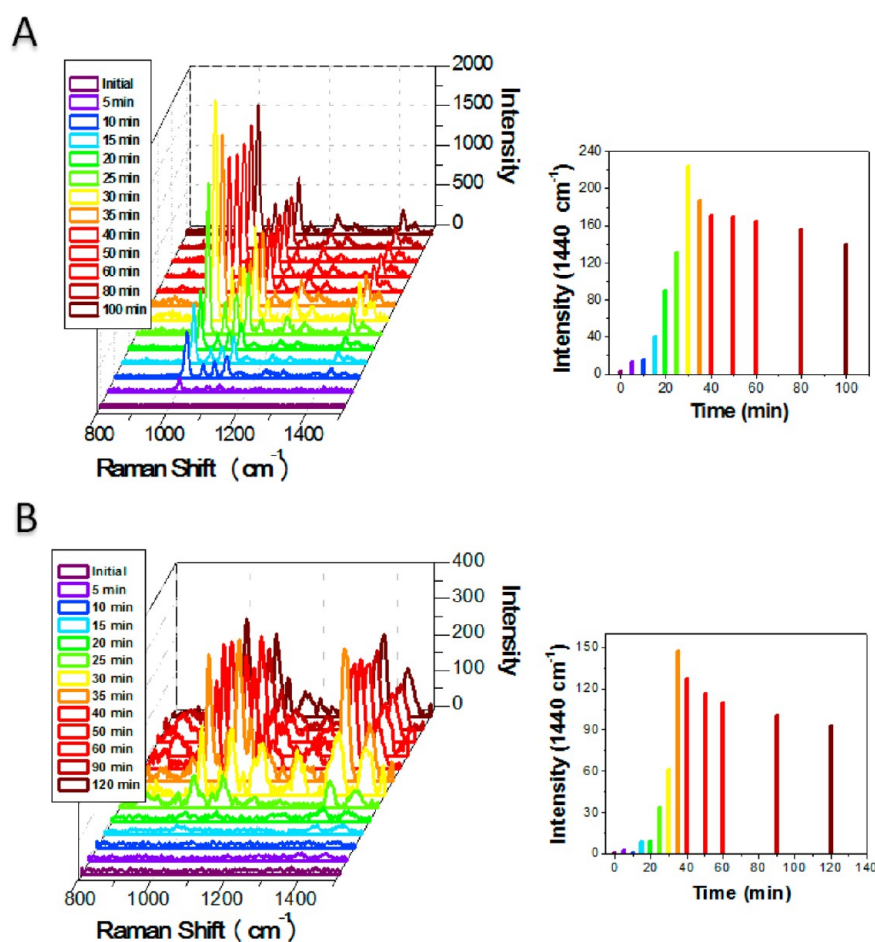
Figure 7. Evolution of the SERS spectra during the aggregation of 56 nm Ag NSs and 90 nm Au NSs. (A) Evolution of the SERS spectra of biotin during the aggregation, at an excitation wavelength $\lambda = 488$ nm, for colloidal dispersions of the 56 nm Ag NSs (left column). Intensity as a function of time for the 1440 cm^{-1} peak at each aggregate time (right column). (B) Evolution of the SERS spectra of biotin during the aggregation, at an excitation wavelength $\lambda = 633$ nm, for colloidal dispersions of the 90 nm Au NS random aggregates. Intensity as a function of time for the 1440 cm^{-1} peak at each aggregate time (right column).
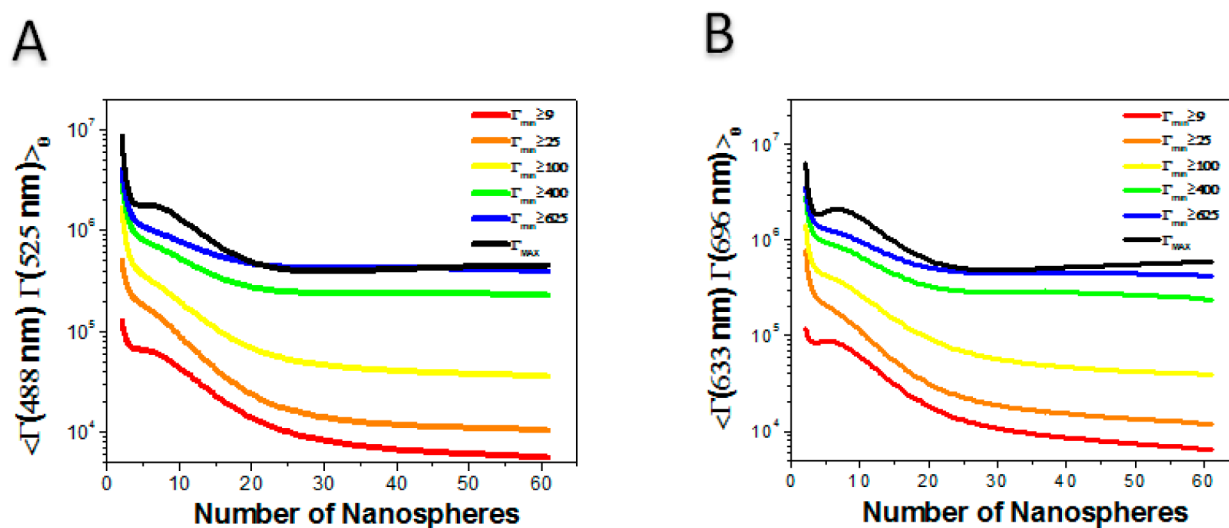

Figure 8. Near-field enhancement simulated for representative clusters. Near-field GMM calculations of the product of the square power of the average E-field enhancement at the incident frequency and the square power of the average field enhancement at the frequency of the 1440 cm^{-1} vibrational mode averaged over several polarizations and considering different minimum values of E-field enhancement for (A) 56 nm diameter Ag NS clusters and (B) 90 nm diameter Au NS clusters, as a function of the number of NSs in the cluster.

Stokes frequency of this particular vibrational mode ($\Gamma(525$ nm) for Ag and $\Gamma(696$ nm) for Au), averaged over different polarization of the external E-field and considering different minimums of enhancement (Γ_{min}) in the calculation of the
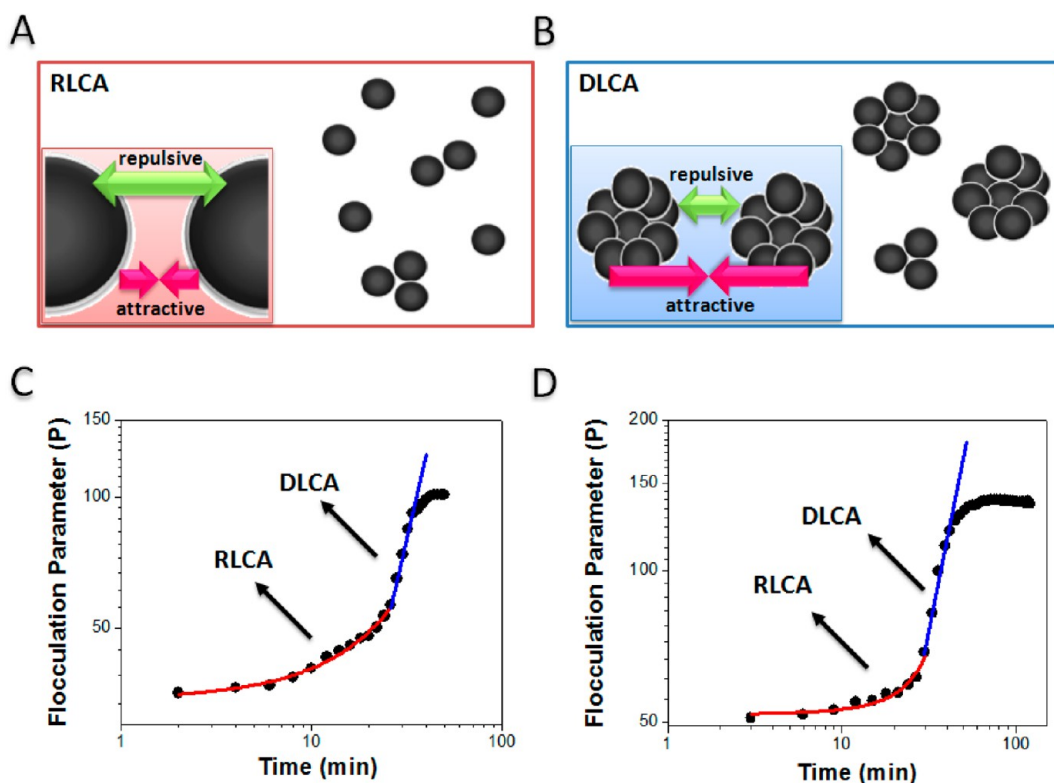
Figure 9. Kinetics of Ag and Au NS aggregation. Schematic illustration of the effective interactions of functionalized metallic colloids in the (A) reaction-limited cluster aggregation (RCLA) regime and (B) the diffusion-limited cluster aggregation (DLCA) regime. Green arrows represent the repulsive interactions, and red arrows represent the attractive interactions. Log−log plots of flocculation parameter (P) as a function of time for (C) Ag NS aggregation and (D) Au NS aggregation. A crossover from RLCA to DLCA is observed in both cases.

$\langle\Gamma(\omega)\rangle_\theta$. As it can be appreciated in Figure 8A and B, for both metals, independent of the lower limit considered for calculating the average, the electromagnetic SERS enhancement factor decreases with the number of NPs in the cluster taking different asymptotic values depending on the value of Γ_{min} considered, except when Γ_{min} corresponds to the maximum near-field enhancement. This trend observed for both metals is in qualitative agreement with the experimental observations of the SERS intensity profile of the 1440 cm^{-1} vibrational mode of biotin during the formation of Ag and Au clusters (see right columns in Figure 7A and B, respectively). For instance, one should be able to explain the significant differences between the maximum experimental SERS intensity reached and the corresponding asymptotic values for Ag and Au clusters since the maximum SERS intensity could be associated with the presence of small clusters (dimers and trimers) in agreement with the theoretical near-field calculations. The fact that there is a maximum in the SERS spectra evolution and then a decay does not imply that in the first stages only dimers are formed, instead a distribution of small clusters. According to DVLO theory the stability of a colloidal dispersion is related to the relative contributions of attractive forces (mainly electrostatic and van der Waals interactions) and repulsive forces (steric and electrostatic repulsion). In the experimental conditions of this work (i.e., functionalization of very few molecules per nanoparticle) a reduction of the effective nanoparticle charge by removal of citrate ions can be rejected. Therefore, it can be assumed that the repulsive forces due to the electrostatic repulsion of the citrate ions adsorbed onto the nanoparticle surface remain almost constant during the functionalization. In this case the agglomeration only occurs through chemical

interactions, i.e., biotin−biotin H-bonds, which in the early stages of the aggregation occur through a kinetic regime where the net potential barrier between colloidal nanoparticles reduces the probability of attachment (i.e., only a small fraction of encounters results in particle aggregation). This behavior is characteristic of reaction-limited cluster aggregation (RLCA) kinetics, which gives rise mainly to the formation of small clusters (see Figure 9A). On the other hand, when the attractive forces due to cluster−cluster interactions are strong enough that the repulsion potential can be compensated (i.e., for relatively large clusters), the dominating attractive potential generates a change of the aggregation regime where now it can be considered that the colloidal nanoparticles stick permanently as soon as they touch, and the whole mechanism is limited by the diffusion time of the particles in the suspension. This behavior is characteristic of diffusion limited cluster aggregation (DLCA) kinetics (see Figure 9B). This is in agreement with the analysis performed above; i.e., in the early stages of aggregation small clusters are the ones that make the most significant contribution to the SERS response, while in the kinetic growth change to a DLCA regime mostly large close-packed clusters are responsible for the SERS behavior.

The aggregation kinetics regime can be characterized by the integral of the extinction intensity, defined as the flocculation parameter (P)[59]

$$P = \int_{\lambda_{min}}^{\lambda_{max}} I_{Ext}(\lambda)\,d\lambda$$

(2)

The time dependence of P could be related to temporal variation of the mean cluster size $S(t)$ whose fitting allows us to
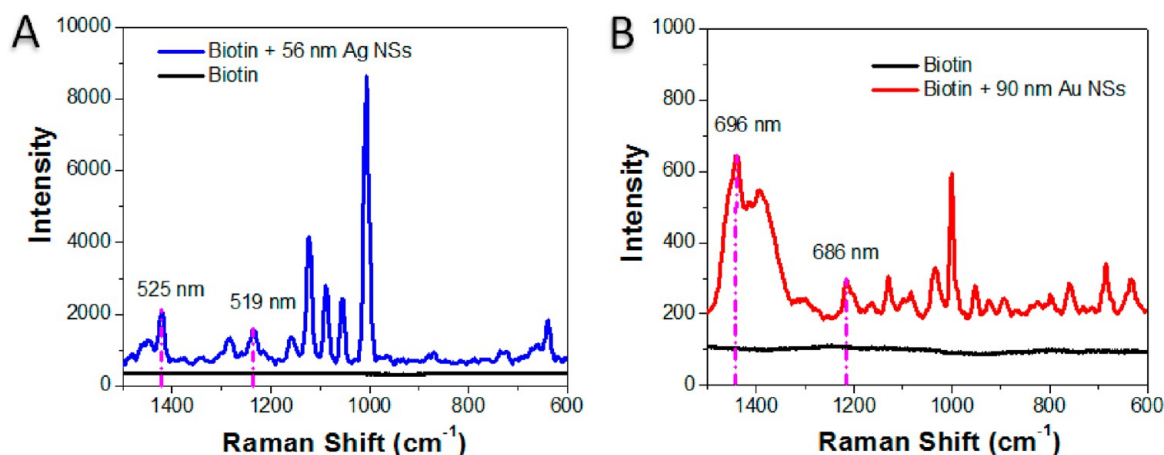
Figure 10. Comparison of the SERS spectrum of biotin in 56 nm Ag NS and 90 nm Au NS aggregate colloidal dispersion and the Raman spectra of biotin in water at picomolar concentration. (A) SERS spectrum of biotin in 56 nm Ag NS aggregate and Raman spectrum of biotin at a 7.59×10^{-12} M concentration. The SERS spectrum was measured after 2 h of the addition of biotin irradiating at $\lambda = 488$ nm. The two wavelengths of the Stokes signals for biotin (525 and 519 nm) are highlighted with dashed lines. (B) SERS spectrum of biotin in 90 nm Au NS aggregates and Raman spectrum of biotin at a 7.24×10^{-12} M concentration. The SERS spectrum was measured after 2 h of the addition of biotin irradiating at $\lambda = 633$ nm. The two wavelengths of the Stokes signals for biotin (696 and 686 nm) are highlighted with dashed lines.

differentiate the kinetic regime (RLCA or DLCA) as they obey different growth laws

$$\text{RCLA: } P(t) \propto S(t) \propto \exp(t/k) \tag{3}$$

$$\text{DCLA: } P(t) \propto S(t) \propto t^{\tau} \tag{4}$$

where τ is considered a constant value and k is the time constant.[59]

To corroborate the kinetic regime crossover observed in the measures of the SERS temporal variation, the temporal variation of the flocculation parameter (P) as a function of time for Ag NS and Au NS aggregation was determined. The corresponding time evolutions of each extinction spectra at different times during NS aggregation are available in the Supporting Information (Figure S2). The wavelength range used to calculate P was from 530 to 1100 nm for Ag NSs and from 700 to 1100 nm for Au NSs, and they were chosen in such a way to cover the whole collective mode of the aggregates. The log–log plots of the temporal variation of the flocculation parameter (P) for Ag NSs and Au NSs are shown in Figure 9C and D, respectively. The analysis of Figure 9C reveals that in the very early stages, within the first 25 min, there is a clear exponential growth in agreement with eq 3 which indicates a RCLA kinetics growth. Following this exponential growth there is a change to a power law behavior kinetics observed as a linear relation in the log–log plot. In the case of Au NSs (see Figure 9D) the exponential growth occurs during the first 30 min, also followed by a linear relation in the log–log plot. This evidence suggests that there is indeed a change of regime from a RCLA to a DCLA kinetic growth, during the nanoparticles aggregation.

Note that there is an excellent correlation between the time in which this change of regime (from RCLA to DCLA) determined from the flocculation parameter and the time when an abrupt change in the graphic of the SERS intensity as a function of time for the 1440 cm^{-1} peak occurs (see Figure 6A and B), which is 25 and 35 min during Ag NS and Au NS aggregation, respectively.

To give a quantitative assessment of the near-field properties, we will now compare the experimental and the theoretical

enhancement values in the asymptotic region (large clusters). For that purpose we will first calculate the analytic enhancement factor (AEF) for Ag and Au clusters, defined as the ratio of the intensity of the SERS signal (I_{SERS}) of a given mode and the intensity of the Raman signal (I_{RS}) of the same mode for a given analyte, both normalized with the respective analyte concentration (C)[50]

$$\text{AEF} = \frac{\dfrac{I_{\text{SERS}}}{C_{\text{SERS}}}}{\dfrac{I_{\text{RS}}}{C_{\text{RS}}}} \tag{5}$$

The experimental SERS signals detected correspond to the contributions of biotin and pyridine-2-thione, as a consequence of the rupture of the disulfide bond in the biotin–HPDP molecule. To select the appropriate vibrational mode for the determination of the AEF, quantum mechanics calculations of the Raman spectra of biotin and pyridine-2-thione were performed (see Supporting Information Figure S3). An excellent correlation between the experimental SERS spectrum generated in the Ag NS aggregate colloidal dispersion and the theoretical Raman spectra was obtained if both biotin and pyridine-2-thione are taken into account; i.e., the SERS spectrum comes from the contribution of both molecules (see Supporting Information Figure S4).

In Figure 10, we compare the SERS spectra obtained for colloidal solutions of Ag and Au NSs aggregates after 1 and 2 h of the addition of biotin, respectively, for excitation at 488 and 633 nm. In this figure we have indicated with dashed lines the two vibrational modes selected for the determination of the AEF at their particular Stokes frequencies: the methylene twisting mode at 1440 cm^{-1} (Stokes frequency at $\lambda = 525$ nm for Ag experiments and $\lambda = 696$ nm for Au experiments) and ureido ring mode at 1221 cm^{-1} (Stokes frequency at $\lambda = 519$ nm for Ag experiments and $\lambda = 686$ nm for Au experiments).

From the theoretical point of view, the main mechanism that produces the SERS effect is the electromagnetic one. According to this mechanism, the electromagnetic field enhancement factor, EFEF, is given by

$$\text{EFEF} = |\Gamma(\omega)||\Gamma(\omega')| \tag{6}$$

Table 1. Experimental and Theoretical SERS Enhancement Factors for 56 nm Ag NS and 90 nm Au NS Aggregates in Aqueous Media for the Detection of Biotin[a]

composition	c/ω (nm)	analyte	$C_{Analyte}$ (M)	intensity (counts)	ν (cm^{-1})	AEF (maximum)	AEF (asymptotic)	c/ω' (nm)	EFEF$_{dimer}$ $\Gamma \geq 100$	EFEF$_{cluster}$ $\Gamma \geq 100$
biotin	488	biotin	6.17×10^{-6}	36	1439	-	-	-	-	-
biotin + Ag NSs	488	biotin	7.59×10^{-12}	420	1440	$(9.5 \pm 0.1) \times 10^6$	-	525	1.69×10^6	-
biotin + Ag NSs	488	biotin	7.59×10^{-12}	234	1440	-	$(5.3 \pm 0.5) \times 10^6$	525	-	3.56×10^4
biotin	488	biotin	6.17×10^{-6}	29	1221	-	-	-	-	-
biotin + Ag NSs	488	biotin	7.59×10^{-12}	680	1224	$(1.9 \pm 0.3) \times 10^7$	-	519	1.70×10^6	-
biotin + Ag NSs	488	biotin	7.59×10^{-12}	256	1224	-	$(7.1 \pm 0.8) \times 10^6$	519	-	3.60×10^4
biotin	633	biotin	9.25×10^{-6}	42	1439	-	-	-	-	-
biotin + Au NSs	633	biotin	7.24×10^{-12}	300	1440	$(9.1 \pm 0.9) \times 10^6$	-	696	1.44×10^6	-
biotin + Au NSs	633	biotin	7.24×10^{-12}	156	1440	-	$(4.7 \pm 0.6) \times 10^6$	696	-	3.93×10^4
biotin	633	biotin	9.25×10^{-6}	39	1221	-	-	-	-	-
biotin + Au NSs	633	biotin	7.24×10^{-12}	222	1217	$(7.3 \pm 0.9) \times 10^6$	-	686	1.48×10^6	-
biotin + Au NSs	633	biotin	7.24×10^{-12}	89	1217	-	$(2.9 \pm 0.6) \times 10^6$	686	-	3.62×10^4

[a]AEF (maximum) = analytic enhancement factor calculated for the maximum in the evolution of the SERS intensity; AEF (asymptotic) = analytic enhancement factor calculated at the plateau in the evolution of the SERS intensity; EFEF$_{Dimer}$ = theoretical enhancement considering the square power of the enhanced field at the incident frequency (ω) multiplied by the square power of the enhanced field at a Stokes frequency (ω') for dimers with a 5 nm gap; EFEF$_{Cluster}$ = theoretical enhancement considering the square power of the enhanced field at the incident frequency (ω) multiplied by the square power of the enhanced field at a Stokes frequency (ω') for a 61-sphere compact nanocluster. All EFEF values were calculated considering the angular average and $\Gamma \geq 100$.

$$|\Gamma(\omega)| = \left(\left| \frac{E(\omega)}{E_0(\omega)} \right| \right)^2 \tag{7}$$

$$|\Gamma(\omega')| = \left(\left| \frac{E(\omega')}{E_0(\omega')} \right| \right)^2 \tag{8}$$

where $|\Gamma(\omega)|$ is the square of the enhanced electric field generated at the frequency of the incident radiation (ω) and $|\Gamma(\omega')|$ is the square of the enhanced electric field generated at a particular Stokes frequency (ω').[32]

The ordinary Raman intensity (I_{RS}) can be written as

$$I_{RS} = F_R \sigma_R C_{RS} \tag{9}$$

where F_R is an instrumental factor; σ_R is the Raman cross section of the free molecule; and C_{RS} is the concentration. The SERS intensity (I_{SERS}) is given by a similar expression but slightly modified to separate out the physical enhancement, i.e., EFEF, from the molecular cross section and other contributions

$$I_{SERS} = F_S \sigma_S C_{SERS} \text{EFEF} \tag{10}$$

where F_S is an instrumental factor; σ_S is the Raman cross section of the molecule on the nanostructure; and C_{SERS} is the concentration on the nanostructure. If we assume that the instrumental factors are the same in both experiments the global SERS enhancement factor (AEF) can be obtained substituting eqs 9 and 10 into eq 5

$$\text{AEF} = (\sigma_S/\sigma_R)\text{EFEF} \tag{11}$$

The ratio σ_S/σ_R could be augmented as a result of the formation of metal−ligand coordination complexes with the surface or by charge transfer transitions.[60] However, these mechanisms alone cannot account for the 10^6-10^8 AEF observed in many experiments. In addition, these mechanisms

are still the subject of considerable research work, but it is now accepted that they can contribute with a factor of $10-100$ to the global AEF.[60]

The average EFEF ($\langle \Gamma(\omega)\Gamma(\omega')\rangle_\theta^{\Gamma_{min}}$) for enhancements greater than Γ_{min} was calculated taking the average of eq 6, considering all the points inside the cluster, according to the following equation

$$\langle \Gamma(\omega)\Gamma(\omega')\rangle_\theta^{\Gamma_{min}} = \int_{\Gamma_{min}}^{\Gamma_{max}} \Gamma_i(\omega)\Gamma_i(\omega')\mathrm{d}i \Big/ \int_{\Gamma_{min}}^{\Gamma_{max}} \mathrm{d}i \tag{12}$$

Nevertheless, it is important to remark that there are two opposite effects in the theoretical estimation of the EFEF with respect to the selected Γ_{min} value: On one hand, increasing the selected Γ_{min} value will lead to a higher average EFEF, which will decrease the difference between the calculated EFEF and the experimental AEF. On the other hand, as Γ_{min} increases the spatial region of the cluster having these values is constrained, which implies a smaller fraction of molecules contributing to the SERS signal. In that sense, for a given Γ_{min} value, the effective average EFEF should take into account this effective number of active molecules. Therefore, the effective EFEF for a given Γ_{min} has to be calculated multiplying the average EFEF by an appropriate fraction. This quantity can be calculated multiplying eq 12 by the fraction (f) of the electromagnetic contribution to the SERS signal coming from all the points having enhancements greater than Γ_{min}

$$f = \int_{\Gamma_{min}}^{\Gamma_{max}} \Gamma_i(\omega)\Gamma_i(\omega')\mathrm{d}i \Big/ \int_{\Gamma_{min}=9}^{\Gamma_{max}} \Gamma_i(\omega)\Gamma_i(\omega')\mathrm{d}i \tag{13}$$

The value $\Gamma_{min} = 9$ in the denominator of eq 13 has been chosen because this value encompasses all the points inside the cluster. Note that if we choose $\Gamma_{min} = 9$ for all the integrals in eqs 12 and 13, the effective EFEF corresponds just to the
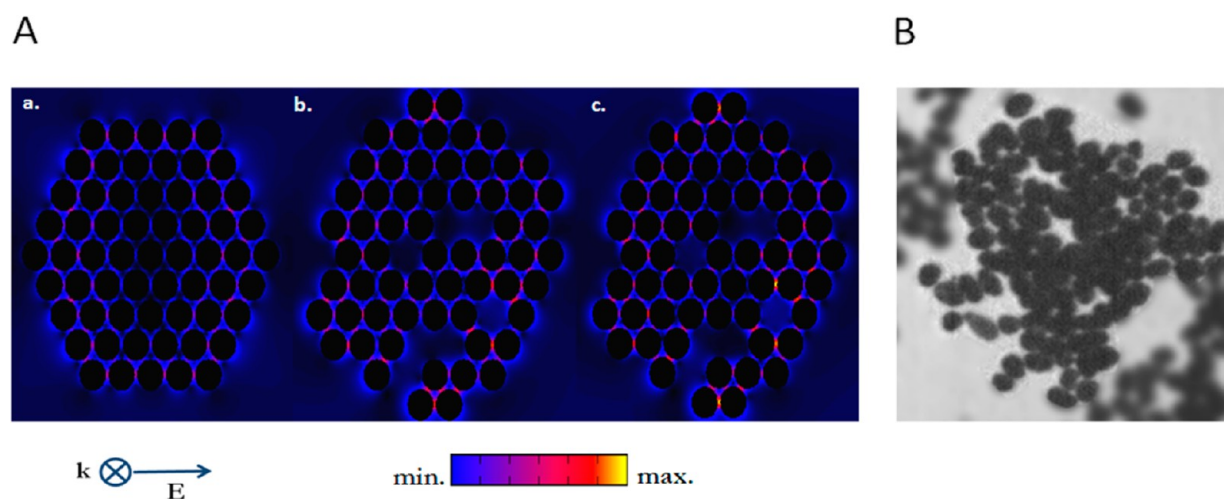
Figure 11. Influence of randomness and gap variability in the near-field optical properties of tight compact nanoclusters. (A) Spatial distribution of *E*-field enhancement at $\lambda = 633$ nm for the 61 NS Au compact nanocluster: 61 NS cluster with an idealized configuration (a), 61 NS cluster with a randomness structure including vacancies (b), 61 NS cluster with a randomness structure including vacancies and the variation of the gap distance (c). (B) Representative TEM image of the close-packed clusters.

average EFEF of the cluster. We have calculated the effective EFEF for different values of Γ_{min} in the range $25 \leq \Gamma_{min} \leq 400$, and it was found that the value varies from 10 000 to 50 000 within this range (see Figure S5 in the Supporting Information). Considering this feature, at this point we will make the comparison between experiments and theory performing the average with $\Gamma_{min} \geq 100$ and taking into account the effective EFEF. The average EFEF was determined for two different cluster models, a dimer and considering a 61 NS close-packed cluster, and the results were compared with the AEF given by eq 5. The comparison was performed for the Stokes signals of biotin at $\lambda = 525$ and $\lambda = 519$ nm for Ag experiments and at $\lambda = 696$ and $\lambda = 686$ nm for Au experiments (highlighted by the vertical lines in Figure 10). The calculated values of the AEF and EFEF$_{\Gamma \geq 100}$ for Ag and Au aggregates and clusters are shown in Table 1. The reference spectrum of biotin used to calculate the AEF according to eq 5 is available in the Supporting Information (Figure S6). There are two features to be remarked: First, there are discrepancies between the experimental AEF with the theoretical enhancement values of biotin in Ag and Au aggregates when both models are considered (the dimer model and the 61 NS cluster model). The ratio between the experimental enhancements (AEF maximum) obtained at the time where the maximum SERS intensity is reached (30 and 35 min for Ag and Au aggregates, respectively) and the EFEF calculated for dimers is a factor of 5−10. In this calculation it has been assumed that, at this stage, the experimental SERS signal is due to the presence of dimers instead of a distribution of small clusters. To asses a more accurate correlation between the EFEF and the SERS response, the asymptotic value of the experimental SERS signals is the suitable region to perform such analysis. In this regime, as has been demonstrated by the theoretical calculations, the EFEF is almost independent of the cluster size. The ratio between the asymptotic AEF and the EFEF for a 61 NS cluster is 149 and 197 for the Stokes signals at $\lambda = 525$ and $\lambda = 519$ nm for Ag clusters and 119 and 80 for the Stokes signals at $\lambda = 696$ nm and at $\lambda = 686$ nm for Au clusters (or 196, 259, 157, and 105 if one considers the effective EFEF, respectively). Other sources that could modify the calculated EFEF besides the angular average are the fluctuations in the interparticle distance and the

presence of vacancies in the cluster geometry. We have performed hundreds of calculations varying in a random fashion the interparticle distance in the range 4 ± 1 nm and also introducing vacancies to have a more realistic model (see Figure 11) of the EFEF contribution to the SERS enhancement. Taking these points into account there is a slight increase of the EFEF by a factor 5−6 (see Table 2). Nevertheless, even

Table 2. Influence of the Presence of Vacancies in the Cluster Geometry and the Variation of the Interparticle Distance in the EFEF[a]

	theoretical enhancement (EFEF$_{cluster}$) $\Gamma \geq 100$			
metal	angular average $(\Gamma(\omega)_\theta)^2$	angular average with vacancies $(\Gamma\langle(\omega)\rangle_{\theta,v})^2$	angular average with vacancies and distance variation $(\langle\Gamma(\omega)\rangle_{\theta,v,d})^2$	AEF (asymptotic)
Ag	5.2×10^4	1.2×10^5	2.8×10^5	$(5.3 \pm 0.5) \times 10^6$
Au	5.0×10^4	9.4×10^4	2.5×10^5	$(4.7 \pm 0.6) \times 10^6$

[a]$\langle\Gamma(\omega)\rangle_\theta$ = theoretical enhancement averaged over 18 different polarizations; $\langle\Gamma(\omega)\rangle_{\theta,v}$ = theoretical enhancement considering simultaneously the average over different polarization and the variation of the cluster geometry by generating vacancies in the cluster in a random way; $\langle\Gamma(\omega)\rangle_{\theta,v,d}$ = theoretical enhancement taking into account simultaneously the average over different polarization, the variation of the cluster geometry by generating vacancies, and the variation of the gap distance between 4 ± 1 nm; AEF (asymptotic) = analytic enhancement factor calculated at the plateau in the evolution of the SERS intensity. All EFEF values were calculated considering the fourth power of the enhanced field at the incident frequency (ω) and $\Gamma \geq 100$.

with these improvements in the model, the ratio AEF/EFEF is still significant being around a factor 19 for both metals (25 if one considers the effective EFEF). As mentioned before, the resulting effective average EFEF varies within a factor of 5 (i.e., between 65 000 and 320 000 in the range $\Gamma_{min} = 25$ to $\Gamma_{min} = 400$, now considering vacancies and varying the interparticle distances), which leads to an upper and a lower effective EFEF value (see Supporting Information Figure S5). Using these upper and lower limit values the ratios AEF/EFEF are 66 and 17, respectively. In that sense, whatever the value of Γ_{min}
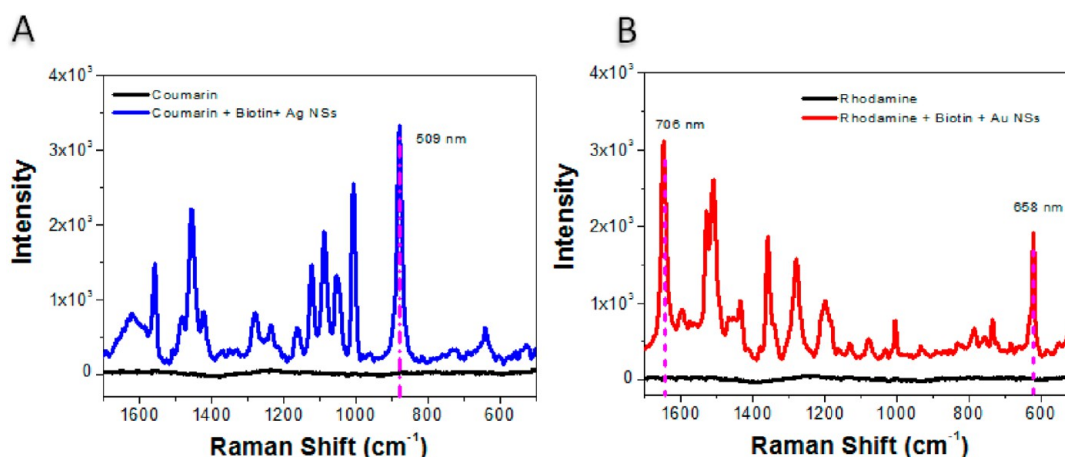
Figure 12. Comparison of the SERS spectrum of Coumarin 440 in 56 nm Ag NS and Rhodamine B in 90 nm Au NS aggregates colloidal dispersion. (A) SERS spectrum of Coumarin 440 in 56 nm Ag NS aggregate and Raman spectrum of Coumarin at a 1×10^{-7} M concentration. The SERS spectra were measured after 2 h of the addition of biotin irradiating at $\lambda = 488$ nm. The wavelength of the Stokes signal for Coumarin (509 nm) is highlighted with dashed lines. (B) SERS spectrum of Rhodamine B in 90 nm Au NS aggregate and Raman spectrum of biotin at a 1×10^{-7} M concentration. The SERS spectrum was measured after 2 h of the addition of biotin irradiating at $\lambda = 633$ nm. The two wavelengths of the Stokes signals for Rhodamine B (706 and 658 nm) are highlighted with dashed lines.

Table 3. Experimental and Theoretical Enhanced Factors in 56 nm Ag NS and 90 nm Au NS SERS Substrates in Aqueous Solution for the Detection of Coumarin 440 and Rhodamine B^a

composition	c/ω (nm)	analyte	$C_{analyte}$ (M)	Raman (counts)	ν (cm^{-1})	AEF	EFEF$_{cluster}$ $\Gamma \geq 9$ $(\langle\Gamma(\omega)\rangle_{\theta,v,d})^2$
CM440	488	CM440	1×10^{-3}	1030	880	-	-
CM440 + biotin + Ag NSs	488	CM440	1×10^{-7}	3484	879	$(3.4 \pm 0.2) \times 10^4$	6.8×10^4
RHB	633	RHB	1×10^{-3}	713	1652	-	-
RHB + Biotin + Au NSs	633	RHB	1×10^{-7}	2178	1647	$(3.1 \pm 0.3) \times 10^4$	5.1×10^4
RHB	633	RHB	1×10^{-3}	1249	613	-	-
RHB + Biotin + Au NSs	633	RHB	1×10^{-7}	1537	621	$(1.2 \pm 0.1) \times 10^4$	5.1×10^4

^{a}RHB = Rhodamine B; CM440 = Coumarin 440; AEF = Analytic enhancement factor; $\langle\Gamma(\omega)\rangle_{\theta,v,d}$ = theoretical enhancement taking into account simultaneously the average over different polarization, of the cluster geometry by generating vacancies, and the variation of the gap distance between 4 ± 1 nm. All EFEF values were calculated considering the fourth power of the enhanced field at the incident frequency (ω) and $\Gamma \geq 9$.

chosen the average effective EFEF is always smaller than the experimentally determined AEF, and this difference could not be explained solely by the EM mechanism. A possible explanation could be that some kind of chemical enhancement is operating. However, the confirmation that this chemical contribution is present would require additional quantum mechanical calculations to have a more quantitative assessment of the ratio σ_S/σ_R for biotin interacting with Ag or Au clusters and for the biotin free molecule, but this is beyond the scope of the present work. Despite this, the fact that the trends in the field enhancement values are maintained for different Γ_{min} values indicates that there is a very good qualitative correlation between theory and experiment considering the complexity of the system under study.

To evaluate if there is a better correlation between AEF and EFEF without having the difficulties involved in the analyses performed above for biotin molecules, additional experiments using two dye molecules (Coumarin 440 and Rhodamine B) as SERS reporters were conducted. These molecules are, in principle, not able to form any covalent interaction with the nanoparticles and therefore should be distributed randomly in the cluster, making the comparison between theory and experiments by far more simple. For such a purpose, once the clusters using biotin molecules as linkers were formed, these dye molecules were added at long enough times (1 and 2 h for Ag and Au experiments, respectively) to ensure that an

asymptotic regime in the SERS response during cluster aggregation has been reached. The dye concentrations were chosen high enough that the average SERS signals could be correlated with the average EFEF. The experimental SERS spectra of Coumarin 440 (CM440) and Rhodamine B (RHB) obtained after being added to Ag and Au cluster solutions are shown in Figure 12. Note these dye molecules were chosen in such a way that any photochemical excitation of the molecules occurs at excitation wavelengths used in the present work (488 and 633 nm for Ag and Au experiments, respectively). The calculated values of the AEF for CM440 and RHB and the EFEF$_{\Gamma \geq 9}$ for 61 NS Ag and Au clusters $((\langle\Gamma(\omega)\rangle_{\theta,v,d})^2)$ are shown in Table 3. As it can be observed in this table, the correlation between experiments and the theoretical calculation has been significantly improved, indicating that for these dye molecules the SERS enhancement can be explained mainly using the theoretical EFEF (EM mechanism) within experimental errors.

Finally, note that even the model used for the calculation can be improved by taking into account polydispersity of NS sizes and 3D effects, the trends observed in the experiments can be qualitatively explained by the theoretical simulations, i.e., the EM mechanism, when biotin is the Raman active molecule and an almost quantitative correlation when dye molecules are used as SERS reporters.

■ CONCLUSIONS

In the present work we have investigated the influence of cluster size on the SERS response of 56 nm diameter silver and 90 nm gold NS aggregates with controlled interparticle gaps generated by biotin−biotin H-bond interactions.

By calculating the variation of the maximum $\|\Gamma\|(\omega)\|$ as a function of wavelength for clusters having a different number of nanospheres, it is possible to choose a wavelength range where this Γ value becomes independent of the number of spheres of the cluster after reaching a critical number. The variation of the angular average follows the same trend observed for the maximum Γ at a single polarization; therefore, this calculation is very helpful to choose the excitation wavelength, even if the correlation is performed without the angular average enhancement of the cluster.

For other wavelength ranges the variation of Γ with the number of spheres could be more complex. Taking into account that at sufficiently long time the populations of these large clusters which give rise to an almost equal enhancement are prevailing, the comparison of the asymptotic value of the SERS AEF with the EFEF is feasible. At any other wavelength or at earlier times this comparison could not be directly performed as it would be necessary to know the cluster size distribution, as each cluster has a different (not constant) contribution to the SERS enhancement. Therefore we propose the following procedure to make a more rigorous and reasonable comparison of the SERS response with electrodynamics simulations:

1. Calculate the MNFES for tight compact clusters of different size (with a controlled and known interparticle gap).
2. Choose a wavelength range where Γ as a function of cluster size reaches a constant value and uses the excitation wavelength for the SERS experiments.
3. Follow the evolution of the SERS enhancement of a particular vibrational mode and verify that it reaches after a given time an almost constant value. This corroborates the theoretical hypothesis that for large enough clusters the SERS signal is independent of the cluster size distribution.

The above methodology seems to be quite suitable as it has been demonstrated for two different noble metal aggregates in the present work by choosing the two excitation wavelengths (488 nm for Ag and 633 nm for Au experiments, respectively) according to the above prescription.

The advantage of using this procedure is that a better assessment of the contribution of the EM mechanism to the SERS response is feasible. In this respect, we found that even though there are differences between the experimental and theoretical enhancement factors the trends in the SERS response of the biotin molecules are qualitatively explained by the EM mechanism for both Ag and Au clusters. Moreover, the analytical SERS enhancements of nonbonded molecules randomly located in the clusters such as CM440 and RHB are in quantitative agreement with that predicted by the EM mechanism.

In addition, experiments performed at low biotin concentrations (on the order of one biotin per NS) allow us to qualitatively explain the trend observed for the evolution of the intensity of the Raman signals, at 488 nm for Ag and 633 nm for Au, in terms of the enhancements in clusters of different size during the aggregation process. In this respect two different kinetic regimes, RLCA and DLCA, determine the cluster size distribution at each stage of the aggregation. The initial growth of the SERS signals is consistent with the generation of small clusters, while the decay is consequence to the formation of large clusters. These results correlate very well with GMM near-field calculations that give rise to a decay of the maximum enhancement as the number of NSs in the cluster increases, for both Ag and Au aggregates, upon a critical size being reached. Beyond this critical size (around 20 nanoparticles) the EFEF is almost constant independent of the number of nanoparticles. This decay of the EFEF with cluster size is consistent with the increasing role played by retardation damping effects for larger clusters. This feature is evidenced in both the extinction spectra by a significant broadening of the LSPR with cluster size and in the red shift of the MNFES with respect to the corresponding extinction spectra for the same cluster size. This effect, however, gives rise to very significant changes in the EFEF by increasing the number of NSs for small clusters, while the effect is by far less significant for large clusters; i.e., the change in the EFEF is so small that it could be considered almost constant after some critical number of spheres in the cluster.

As a final remark, the present results demonstrate the importance of generating small clusters (dimers and trimers) rather than large aggregates, if one wishes to optimize the SERS response for ultrasensitive detection, tuning at the appropriate excitation wavelength according to the MNFES.

■ ASSOCIATED CONTENT

ⓈSupporting Information

Maximum near-field enhancements of 56 nm Ag and 90 nm Au clusters at different wavelengths; Evolution of the extinction spectra during Ag and Au aggregation for determining the kinetics of the agglomeration process and determining the Flocculation Parameter (P); Quantum chemistry calculations of biotin and pyridine-2-thione Raman spectra; Spectroscopic assignment of the contribution of each molecule to the experimental SERS spectrum; Calculation of the effective EFEF as a function of the Γ_{min}; Reference Raman spectrum of biotin at 6.17×10^{-6} M and 9.25×10^{-6} M. This material is available free of charge via the Internet at http://pubs.acs.org.

■ AUTHOR INFORMATION

Corresponding Author
*E-mail: coronado@fcq.unc.edu.ar.
Author Contributions
All authors contributed equally to this work.
Notes
The authors declare no competing financial interest.

■ ACKNOWLEDGMENTS

■ REFERENCES

(1) Stiles, P. L; Dieringer, J. A.; Shah, N. C.; Van Dyune, R. P. Surface-Enhanced Raman Spectroscopy. *Annu. Rev. Anal. Chem.* **2008**, *1*, 601−626.

(2) Bruno Pettinger, B.; Schambach, P.; Villagómez, C. J.; Scott, N. Tip-Enhanced Raman Spectroscopy: Near-Fields Acting on a Few Molecules. *Annu. Rev. Phys. Chem.* **2012**, *63*, 379−399.

(3) Gill, R.; Tian, L.; Somerville, W. R. C.; Le Ru, E. C.; Amerongen, H.; Subramaniam, V. Silver Nanoparticle Aggregates as Highly

Efficient Plasmonic Antennas for Fluorescence Enhancement. *J. Phys. Chem. C* **2012**, *116*, 16687−16693.

(4) Le Ru, E. C.; Etchegoin, P. G. Single-molecule Surface-Enhanced Raman Spectroscopy. *Annu. Rev. Phys. Chem.* **2012**, *63*, 65−87.

(5) Futamata, M.; Maruyama, Y.; Ishikawa, M. *Microscopic Morphology and SERS Activity of Ag Colloidal Particles*; Elsevier: New York, 2002.

(6) Schwartzberg, A. M.; Grant, C. D.; Wolcott, A.; Talley, C. E.; Huser, T. R.; Bogomolni, R.; Zhang, J. Z. Unique Gold Nanoparticle Aggregates as a Highly Active Surface-Enhanced Raman Scattering Substrate. *J. Phys. Chem. B* **2004**, *108*, 19191−19197.

(7) Futamata, M.; Maruyama, Y.; Ishikawa, M. Critical Importance of the Junction in Touching Ag Particles for Single Molecule Sensitivity in SERS. *J. Mol. Struct.* **2005**, *735*, 75−84.

(8) Kneipp, K.; Kneipp, H.; Kneipp, J. Surface-Enhanced Raman Scattering in Local Optical Fields of Silver and Gold Nano-aggregatess—from Single-molecule Raman Spectroscopy to Ultra-sensitive Probing in Live Cells. *Acc. Chem. Res.* **2006**, *39*, 443−450.

(9) Zhao, L. L.; Jensen, L.; Schatz, G. C. Surface-Enhanced Raman Scattering of Pyrazine at the Junction Between Two Ag-20 Nanoclusters. *Nano Lett.* **2006**, *6*, 1229−1234.

(10) Meyer, M.; Le Ru, E. C.; Etchegoin, P. G. Self-Limiting Aggregation Leads to Long-Lived Metastable Clusters in Colloidal Solutions. *J. Phys. Chem. B* **2006**, *110*, 6040−6047.

(11) Fraire, J. C.; Pérez, L. A.; Coronado, E. A. Rational Design of Plasmonic Nanostructures for Biomolecular Detection: Interplay between Theory and Experiments. *ACS Nano* **2012**, *6*, 3441−3452.

(12) Lim, D.-K.; Jeon, K.-S.; Kim, H. M.; Nam, J.-M.; Suh, Y.-D. Nanogap-engineerable Raman-active Nanodumbbells for Single-molecule Detection. *Nat. Mater.* **2010**, *9*, 60−67.

(13) Halas, N. J.; Lal, S.; Chang, W.-S.; Link, S.; Nordlander, P. Plasmons in Strongly Coupled Metallic Nanostructures. *Chem. Rev.* **2011**, *111*, 3913−3961.

(14) Braun, G. B.; Lee, S. J.; Laurence, T.; Fera, N.; Fabris, L.; Bazan, G. C.; Moskovits, M.; Reich, N. O. Generalized Approach to SERS-Active Nanomaterials via Controlled Nanoparticle Linking, Polymer Encapsulation, and Small-Molecule Infusion. *J. Phys. Chem. C* **2009**, *113*, 13622−13629.

(15) Kumar, J.; Thomas, K. G. Surface-Enhanced Raman Spectroscopy: Investigations at the Nanorod Edges and Dimer Junctions. *J. Phys. Chem. Lett.* **2011**, *2*, 610−615.

(16) Hofmann, A.; Schmiel, P.; Stein, B.; Graf, C. Controlled Formation of Gold Nanoparticle Dimers Using Multivalent Thiol Ligands. *Langmuir* **2011**, *27*, 15165−15175.

(17) Talley, C. E.; Jackson, J. B.; Oubre, C.; Grady, N. K.; Hollars, C. W.; Lane, S. M.; Huser, T. R.; Nordlander, P.; Halas, N. J. Surface-Enhanced Raman Scattering from Individual Au Nanoparticles and Nanoparticle Dimer Substrates. *Nano Lett.* **2005**, *5*, 1569−1574.

(18) McLellan, J. M.; Li, Z.-Y.; Siekkinen, A. R.; Xia, Y. The SERS Activity of a Supported Ag Nanocube Strongly Depends on Its Orientation Relative to Laser Polarization. *Nano Lett.* **2007**, *7*, 1013−1017.

(19) Wiley, B. J.; Chen, Y.; McLellan, J. M.; Xiong, Y.; Li, Z.-Y.; Ginger, D.; Xia, Y. Synthesis and Optical Properties of Silver Nanobars and Nanorice. *Nano Lett.* **2007**, *7*, 1032−1036.

(20) Mock, J. J.; Norton, S. M.; Chen, S.-Y.; Lazarides, A. A.; Smith, D. R. Electromagnetic Enhancement Effect Caused by Aggregation on SERS-Active Gold Nanoparticles. *Plasmonics* **2011**, *6*, 113−124.

(21) Kelly, K. L.; Coronado, E. A.; Zhao, L. L.; Schatz, G. C. The Optical Properties of Metal Nanoparticles: The Influence of Size, Shape, and Dielectric Environment. *J. Phys. Chem. B* **2003**, *107*, 668−677.

(22) Perassi, E. M.; Hernandez-Garrido, J. C.; Moreno, M. S.; Encina, E. R.; Coronado, E. A.; Midgley, P. A. Using Highly Accurate 3D Nanometrology to Model the Optical Properties of Highly Irregular Nanoparticles: A Powerful Tool for Rational Design of Plasmonic Devices. *Nano Lett.* **2010**, *10*, 2097−2104.

(23) Kambhampati, P.; Child, C. M.; Foster, M. C.; Campion, A. On the Chemical Mechanism of Surface Enhanced Raman Scattering: Experiment and Theory. *J. Chem. Phys.* **1998**, *108*, 5013−5026.

(24) Li, S.; Pedano, M. L.; Chang, S.-H.; Mirkin, C. A.; Schatz, G. C. Gap Structure Effects on Surface-Enhanced Raman Scattering Intensities for Gold Gapped Rods. *Nano Lett.* **2010**, *10*, 1722−1727.

(25) Su, K. H.; Wei, Q. H.; Zhang, X.; Mock, J. J.; Smith, D. R.; Schultz, S. Interparticle Coupling Effects on Plasmon Resonances of Nanogold Particles. *Nano Lett.* **2003**, *3*, 1087−1090.

(26) Jiang, J.; Bosnick, K.; Maillard, M.; Brus, L. Single Molecule Raman Spectroscopy at the Junctions of Large Ag Nanocrystals. *J. Phys. Chem. B* **2003**, *107*, 9964−9972.

(27) Gunnarsson, L.; Bjerneld, E. J.; Xu, H.; Petronis, S.; Kasemo, B.; Kall, M. Interparticle Coupling Effects in Nanofabricated Substrates for Surface-Enhanced Raman Scattering. *Appl. Phys. Lett.* **2001**, *78*, 802−804.

(28) Jain, P. K.; El-Sayed, M. A. Surface Plasmon Coupling and Its Universal Size Scaling in Metal Nanostructures of Complex Geometry: Elongated Particle Pairs and Nanosphere Trimers. *J. Phys. Chem. C* **2008**, *112*, 4954−4960.

(29) Rechberger, W.; Hohenau, A.; Leitner, A.; Krenn, J. R.; Lamprecht, B.; Aussenegg, F. R. Optical Properties of Two Interacting Gold Nanoparticles. *Opt. Commun.* **2003**, *220*, 137−141.

(30) Xu, H. X.; Aizpurua, J.; Kall, M.; Apell, P. Electromagnetic Contributions to Single-molecule Sensitivity in Surface-Enhanced Raman Scattering. *Phys. Rev. E* **2000**, *62*, 4318−4324.

(31) Le Ru, E.; Etchegoin, P. G. *Principles of Surface Enhanced Raman Spectroscopy*; Elsevier: Amsterdam, 2009; Vol. 1.

(32) Perassi, E. M.; Coronado, E. A. The Structure, Energy, Confinement, and Enhancement of Hot Spots between Two Nanoparticles. *J. Phys. Chem. C* **2013**, *117*, 7744−7750.

(33) Henry, A.-I.; Bingham, J. M.; Ringe, E.; Marks, L. D.; Schatz, G. C.; Van Duyne, R. P. Correlated Structure and Optical Property Studies of Plasmonic Nanoparticles. *J. Chem. Phys.* **2011**, *115*, 9291−9305.

(34) Romo-Herrera, J. M.; Alvarez-Puebla, R. A.; Marzan, L. M. Controlled Assembly of Plasmonic Colloidal Nanoparticle Clusters. *Nanoscale* **2011**, *3*, 1304−1315.

(35) Haes, A. J.; Haynes, C. L.; MacFarland, A. D.; Schatz, G. C.; Van duyne, R. P.; Zou, S. Plasmonic Materials for Surface-Enhanced Sensing and Spectroscopy. *MRS Bull.* **2005**, *30*, 368−375.

(36) Lal, S.; Link, S.; Halas, N. J. Nano-optics from Sensing to Waveguiding. *Nat. Photonics* **2007**, *1*, 641−648.

(37) Lazarides, A. A.; Schatz, G. C. DNA-Linked Metal Nanosphere Materials: Structural Basis for the Optical Properties. *J. Phys. Chem. B* **2000**, *104*, 460−467.

(38) Stockman, M. I.; Shalaev, V. M.; Moskovits, M.; Botet, R.; George, T. F. Enhanced Raman Scattering by Fractal Clusters: Scale-invariant Theory. *Phys. Rev. B* **1992**, *46*, 2821−2830.

(39) Zuloaga, J.; Nordlander, P. On the Energy Shift between Near-field and Far-field Peak Intensities in Localized Plasmon Systems. *Nano Lett.* **2011**, *11*, 1280−1283.

(40) Brown, L. V.; Sobhani, H.; Lassiter, J. B.; Nordlander, P.; Halas, N. J. Heterodimers: Plasmonic Properties of Mismatched Nanoparticle Pairs. *ACS Nano* **2010**, *4*, 819−832.

(41) Sonnichsen, C.; Reinhard, B. M.; Liphardt, J.; Alivisatos, A. P. A Molecular Ruler Based on Plasmon Coupling of Single Gold and Silver Nanoparticles. *Nat. Biotechnol.* **2005**, *23*, 741−745.

(42) Nordlander, P.; Oubre, C.; Prodan, E.; Li, K.; Stockman, M. I. Plasmon Hybridization in Nanoparticle Dimers. *Nano Lett.* **2004**, *4*, 899−903.

(43) Yang, S. C.; Kobori, H.; He, C. L.; Lin, M. H.; Chen, H. Y.; Li, C. C.; Kanehara, M.; Teranishi, T.; Gwo, S. Plasmon Hybridization in Individual Gold Nanocrystal Dimers: Direct Observation of Bright and Dark Modes. *Nano Lett.* **2010**, *10*, 632−637.

(44) Wang, J.; Yang, L.; Boriskina, S.; Yan, B.; Reinhard, B. M. Spectroscopic Ultra-Trace Detection of Nitroaromatic Gas Vapor on Rationally Designed Two-Dimensional Nanoparticle Cluster Arrays. *Anal. Chem.* **2011**, *83*, 2243−2249.

(45) Yan, B.; Boriskina, S. V.; Reinhard, B. M. Optimizing Gold Nanoparticle Cluster Configurations ($n \geq 7$) for Array Applications. *J. Phys. Chem. C* **2011**, *115*, 4578−4583.

(46) Ye, J.; Wen, F.; Sobhani, J.; Lassiter, J. B.; Van Dorpe, P.; Nordlander, P.; Halas, N. J. Plasmonic Nanoclusters: Near Field Properties of the Fano Resonance Interrogated with SERS. *Nano Lett.* **2012**, *12*, 1660−1667.

(47) Rahmani, M.; Lei, D. Y.; Giannini, V.; Lukiyanchuk, B.; Ranjbar, M.; Fook Liew, T. Y.; Hong, M.; Maier, S. A.; Subgroup. Decomposition of Plasmonic Resonances in Hybrid Oligomers: Modeling the Resonance Lineshape. *Nano Lett.* **2012**, *12*, 2101−2106.

(48) Girard, C.; Dujardin, E.; Li, M.; Mann, S. Theoretical Near-field Optical Properties of Branched Plasmonic Nanoparticle Networks. *Phys. Rev. Lett.* **2006**, *97*, 100801−100804.

(49) Taylor, R. W.; Lee, T.-C.; Sherman, O. A.; Esteban, R.; Aizpurua, J.; Huang, F. M.; Baumberg, J. J.; Mahajan, S. Precise Subnanometer Plasmonic Junctions for SERS within Gold Nanoparticle Assemblies Using Cucurbit[n]uril "Glue". *ACS Nano* **2011**, *5*, 3878−3887.

(50) Le Ru, E. C.; Blackie, E.; Meyer, M.; Etchegoin, P. G. Surface Enhanced Raman Scattering Enhancement Factors: A Comprehensive Study. *J. Phys. Chem. C* **2007**, *111*, 13794−13803.

(51) Encina, E. R.; Coronado, E. A. On the Far Field Optical Properties of Ag−Au Nanosphere Pairs. *J. Phys. Chem. C* **2010**, *114*, 16278−16284.

(52) Encina, E. R.; Coronado, E. A. Plasmon Coupling in Silver Nanosphere Pairs. *J. Phys. Chem. C* **2010**, *114*, 3918−3923.

(53) Encina, E. R.; Coronado, E. A. Near Field Enhancement in Ag Au Nanospheres Heterodimers. *J. Phys. Chem. C* **2011**, *115*, 15908−15914.

(54) Palik, E. D. *Handbook of Optical Constants of Solids*; Academic Press: New York, 1985.

(55) Frisch, M. J.; Trucks, G. W.; Schlegel, H. B.; Scuseria, G. E.; Robb, M. A.; Cheeseman, J. R.; Zakrzewski, V. G.; Montgomery, J. A., Jr.; Stratmann, R. E.; Burant, J. C.; et al. *Gaussian 98*, Revision A.7; Gaussian, Inc.: Pittsburgh, PA, 1998.

(56) Coronado, E. A.; Encina, E. R.; Stefani, F. D. Optical Properties of Metallic Nanoparticles: Manipulating Light, Heat and Forces at the Nanoscale. *Nanoscale* **2011**, *3*, 4042−4059.

(57) Marhaba, S.; Bachelier, G.; Bonnet, C.; Broyer, M.; Cottancin, E.; Grillet, N.; Lermé, J.; Vialle, J.-L.; Pellarin, M. Surface Plasmon Resonance of Single Gold Nanodimers Near the Conductive Contact Limit. *J. Phys. Chem. C* **2009**, *113*, 4349−4356.

(58) Park, S.-J.; Lazarides, A. A.; Storhoff, J. J.; Pesce, L.; Mirkin, C. A. The Structural Characterization of Oligonucleotide-Modified Gold Nanoparticle Networks Formed by DNA Hybridization. *J. Phys. Chem. B* **2004**, *108*, 12375−12380.

(59) Zhang, F.; Dressen, D. G.; Skoda, M. W. A.; Jacobs, R. M. J.; Zorn, S.; Martin, R. A.; Martin, C. M.; Clark, G. F.; Schreiber, F. Gold Nanoparticles Decorated with Oligo(ethylene glycol) Thiols: Kinetics of Colloid Aggregation Driven by Depletion Forces. *Eur. Biophys. J.* **2008**, *37*, 551−561.

(60) Moskovits, M. Persistent Misconceptions Regarding SERS. *Phys. Chem. Chem. Phys.* **2013**, *15*, 5301−5311.